Maximum Likelihood Retrieval of Volcanic Ash Concentration and Particle Size from Ground-based Scanning Lidar

L. Mereu[1, 5], S. Scollo[2], S. Mori[1, 5], A. Boselli[3], G. Leto[4], F.S. Marzano[1, 5], *Fellow, IEEE*

[1] *DIET, Sapienza University of Rome, Rome, Italy*
[2] *Istituto Nazionale di Geofisica e Vulcanologia, Osservatorio Etneo, Catania, Italy*
[3] *CNISM and IMAA - Consiglio Nazionale delle Ricerche, Potenza, Italy*
[4] *Istituto Nazionale di Astrofisica-Osservatorio Astrofisico di Catania, Catania, Italy*
[5] *Center of Excellence CETEMPS, University of L'Aquila, L'Aquila, Italy*
E-mail: *mereu@diet.uniroma1.it, frank.marzano@uniroma1.it*

Abstract. **An inversion methodology, named Maximum Likelihood Volcanic Ash Lidar Retrieval (VALR-ML), has been developed and applied to estimate volcanic ash particle size, and ash mass concentration within volcanic plumes. Both estimations are based on the maximum likelihood approach, trained by a polarimetric backscattering forward model coupled with a Monte Carlo ash microphysical model. The VALR-ML approach is applied to lidar backscattering and depolarization profiles, measured at visible wavelength during two eruptions of Mt. Etna (Italy) in 2010 and 2011. Results are compared with ash products derived from other parametric retrieval algorithms. A detailed comparison among these different retrieval techniques highlights the potential of VALR-ML to determine, on the basis of a physically-consistent approach, the ash cloud area that must be interdicted to flight operations. Moreover, the results confirm the usefulness of operating scanning lidars near active volcanic vents.**

Keywords - Explosive eruption, scanning lidar, backscattering and depolarization, retrieval algorithms, volcanic ash concentration, ash mean size.

I. INTRODUCTION

An explosive volcanic eruption can cause a variety of severe and widespread threats to human well-being and the environment [3], [1], [12]. The ash produced during explosive eruptions, has a huge impact on the global environment. Major eruptions strongly influence the Earth's radiative balance by injecting into the atmosphere a large quantity of particles and gases, which produce secondary aerosols [18]. Although the concentration of stratospheric volcanic aerosols is usually very low and rare, they can have notable impact on global climate due to their large-scale dispersion and residence times in the order of months or even several years. By contrast, the residence time of volcanic aerosols in the troposphere is only in the order of several days or months depending on the eruption intensity and duration. Furthermore, its spatial distribution can be rather inhomogeneous, affected mainly by the eruption and atmospheric variability, so that the assessment of their radiative effects is much more complicated [10]. Volcanic ash is critical information for the flight safety of jet-driven aircrafts. Indeed, due to their low melting temperature and their sharp-edged shapes, ash particles can severely damage the turbines and again here and front windows of aircraft [29], [4], [21], [2]. The ash concentration in the atmosphere is an important parameter that needs to be detected with some accuracy [42], because air traffic must be suspended in the regions in which volcanic ash concentrations exceed certain thresholds [10], [11].

In recent years, lidar (light detection and ranging) systems have been widely used to study volcanic aerosol clouds produced by major volcanic eruptions [22]. Lidar techniques are a powerful method for monitoring the dispersion of a volcanic cloud in the atmosphere because of their profiling capability at very high range resolution. A lidar can measure not only backscatter, but also depolarization once two-way path attenuation is properly corrected. Lidar observations can provide plume geometrical properties (i.e., top, bottom, and thickness), its optical depth, aerosol category and also aerosol microphysical properties if advanced multi-wavelength Raman lidar systems are used [45]. Using the depolarization channel, it is also possible to distinguish various shapes of ash particles ([10], [12]).

The capability of lidar systems to detect the finest particles in volcanic plume and reliably estimate the ash concentration mainly depends on instrumental characteristics and the type of explosive activity. For typical ground-based dual-polarized lidars, the evaluation of the aerosol backscattering and depolarization coefficients may be carried out only in those regions where the lidar signal is not extinguished inside the volcanic plume optical thickness. In these cases, assuming the knowledge of the lidar ratio between extinction and backscattering, path attenuation correction algorithms can be applied to reconstruct the effective lidar observable [22]. Optically thick plumes can strongly attenuate the lidar beam, reducing its penetration capability due to absorption effects. Inversion approaches can mitigate the effect of path attenuation by reconstructing the backscatter profile if the return signal is detectable [15], [7]. On the other hand, lidar beam divergence is generally very small (about a few m^3 at ranges of tens of km) so that they can have a better spatial resolution than a radar microwave system, even though at the expense of a smaller wide-area search capability. Multiple scattering is a further effect that can impact the ash retrieval due to the apparent

increase of the return power [46], [47]. However, for relatively low attenuation and/or highly directive lasers close to the explosive volcanic source, the multiple scattering tends to be negligible.

Lidar sensors with scanning capability, installed a few kilometers away from the summit craters, can be valid supports in monitoring the finest airborne ash particles that are rapidly dispersed by the prevailing wind. Lidar measurements near an active volcano are crucial for continuous monitoring of long-lived explosive activity and improving the volcanic ash plume forecast during volcanic crises; nevertheless, lidar systems can be seriously damaged by ash fallout if not properly protected. The measurements near Etna volcano, in Italy, one of the most active volcanoes on Earth, were performed with the Volcanic Ash Monitoring by Polarisation (VAMP) lidar [43]. The VAMP system is a portable dual-polarized lidars with scanning capabilities, allowing detecting elastic backscattered radiation at 532 nm [22]. This system is able to provide highly accurate measurements of the backscatter coefficient and low depolarization ratio with a range resolution of 60 m and azimuth resolution of 1 degree. Whereas water clouds and fog contain spherical liquid droplets exhibiting low aersosol depolarization values, volcanic ash particles are generally asymmetrical associated to high aerosol depolarization values. The latter is readily detected by the VAMP system thanks to its dual polarization channels. Some recent eruptions of Etna volcano were extensively observed by the VAMP system. The calibration of the VAMP system and a detailed description of the apparatus is reported in [22] and [32]. These observations have opened the possibility to validate the scanning mode of lidar instruments and, now, to test different retrieval approaches of ash properties.

The main goals of this work are: i) to introduce the maximum-likelihood volcanic ash lidar retrieval (VALR-ML) based on a Monte Carlo microphysically-oriented backscattering polarimetric forward model. The overall numerical model, called Hydrometeor-Ash Particle Ensemble Scattering Simulator (HAPESS), takes into account the physical and electromagnetic behavior of ash particle polydispersions in a statistical way; ii) to apply the VALR-ML algorithm to the VAMP data collected during two different explosive events of Etna volcano: a prolonged ash emission activity occurring in 2010 at the North East Crater, and during a lava fountain in 2011 at the New South East Crater. The VALR-ML algorithm results are compared with ash concentration estimations, obtained from a parametric retrieval model to evaluate the impact of choosing different approaches for ash-mass no-flight zone contouring [22], [33], [30].

The paper is organized as follows. Sect. II illustrates the lidar polarimetric data processing technique, focusing on the numerical forward model, simulation of lidar observables (also reported in the Appendix) and maximum-likelihood retrieval methodology. Sect. III focuses on the application of VALR-ML to the two Etna eruptions in 2010 and 2011 and on the comparison of results with those obtained by other parametric retrieval algorithms. Section IV draws the conclusions and sets out future work.

II. Polarimetric Lidar Data Processing

The physical approach to lidar remote sensing requires developing a microphysical model that takes into account the volcanic particles features (size, density, shape, refractivity) and its associated backscattering polarimetric response. This forward model can then be used to approach the inverse problem by training an estimation algorithm by means of a set of realistic randomly-generated simulations of the forward model itself. This physical-statistical approach should tackle the issues of non-uniqueness and uncertainty, which affect any remote sensing problem.

A. Volcanic particles lidar model

The microphysical-electromagnetic forward model summarizes the ash particle features, derived from available experimental data and considered as *a priori* information to constrain the inverse solution [35]. The main microphysical properties of ash particle useful for modeling are: i) particle size distribution (PSD); ii) density; iii) angular orientation; iv) axial ratio in case of spheroidal shapes; v) relative dielectric constant models for the frequency/wavelength of interest [16].

The optical lidar response is mainly determined by the PSD of each microphysical species within the detected range volume. The PSD is usually modeled either through a normalized Gamma or Weibull size distribution. In the case of a multi-mode size distribution, it is always possible to suppose more than one analytical PSD characterized by different mean size and total number of particles. We adopt the Scaled-Gamma (SG) PSD as a general model both for ash and hydrometeor particles modeled as a polydispersion of randomly-oriented spheroidal particles [17]. If r is the radius of a volume-equivalent spherical particle (i.e. a sphere whose volume is equivalent to the associated spheroidal particle), the SG PSD N_p, for a generic class of ash particles p, can be written as:

$$N_p(r) = N_{np}\left(\frac{r}{r_{np}}\right)^{\mu_p} e^{-\Lambda_{np}\left(\frac{r}{r_{np}}\right)} \qquad (1)$$

where r_{np} is the number-weighted mean radius, whereas the "intercept" parameter N_{np} and the "slope" parameter Λ_{np} in a logarithmic plane are related to the "shape" parameter μ_p and to the particle density ρ_p, as shown in [49]. If particles are volume-equivalent spheres, their mass is $m_p = \rho_p \cdot (4\pi/3) \cdot r^3$ with a constant density ρ_p; ii) the minimum and maximum radius are 0 and infinite so that the complete moment m_{np} of order n of N_p, can be expressed by:

$$m_{np} = \frac{N_{np}\left(2r_{np}\right)^{n+1}}{\Lambda_{np}^{n+\mu_p+1}}\Gamma(n+\mu_p+1) \qquad (2)$$

where $\Gamma(n+1) = n!$ if n is an integer. Using the previous equation, the total volumetric number of particles N_{tp} [m^{-3}] is $N_{tp} = m_{0p}$, whereas the mass concentration C_p [mg/m^3] is given by $C_p = \pi/6 \cdot \rho_p \cdot m_{3p}$ and the number-weighted particle mean radius r_{np} [μm] is defined by $r_{mp} = m_{1p} / m_{0p}$.

$$\begin{cases} C_p = \int_0^\infty \frac{4}{3}\pi r^3 \rho_p(r) N_p(r) dr = \frac{4}{3}\pi\rho_p m_3 \\ r_{np} = \frac{\int_0^\infty r N(r) dr}{\int_0^\infty N(r) dr} = \frac{m_1}{m_0} = \frac{D_{np}}{2} \end{cases} \qquad (3a)$$

where

$$r_{ep} = \frac{\int_0^\infty r^3 N_p(r)dr}{\int_0^\infty r^2 N_p(r)dr} = \frac{m_3}{m_2} = (\frac{m_3}{m_2}\ \frac{m_0}{m_1}) r_{np} \quad (3b)$$

r_{ep} being the effective radius [μm], expressed as a ratio between the third and second moment of N_p, proportional to the number-weighted particle mean radius r_{np} and its associated mean diameter D_{np}.

For general purposes, we can define a number of ash classes with respect to their average size. It is worth noting that the following size discrimination differs to the one usually adopted by volcanologists [25], [37]. The following ash-diameter classes are identified (as integer powers of 2): i) very fine ash (VA) with mean equivalent diameters between 2^{-3} - 2^3 μm; ii) fine ash (FA) between 2^3 - 2^6 μm; iii) coarse ash (CA) between 2^6 - 2^9 μm; iv) small lapilli (SL) between 2^9 - 2^{12} μm; v) large lapilli (LL) between 2^{12} - 2^{15} μm. Each diameter class may be subdivided with respect to other main parameters, e.g. the ash concentration, orientation angle and axis ratio. The model of ash particle properties is completed by considering the following sets of ash sub-classes, listed in Table I: i) 5 classes for 4 different ash concentrations (i.e. very small =VC, small=SC, moderate=MC, intense=IC and uniform=UC, where the latter includes all previous ones); ii) 5 classes for 5 different orientations (i.e. tumbling with θ=30°=TO.1, tumbling with θ=45°=TO.2, tumbling with θ=60°=TO.3, oblate=OO; prolate=PO); iii) 5 classes for 2 different axis ratio models (RB: Ratio Basaltic-andesitic, RR: Ratio Rhyolitic), even though we have here selected only the RB case considering the particle features from Etna (see also [17], [6]). Considering all combinations, we can obtain sub-classes for each size class. In general, we can list 5 x 4 x 5 x 2 = 200 sub-classes if VC, SC, MC and IC are considered, 5 x 1 x 5 x 2 = 50 sub-classes if UC is considered. A priori information about the volcanic scenario allows tailoring the overall simulations dataset in terms of contributing sub-classes.

The goal, as mentioned, is to build a dataset of simulated lidar observables, obtained with a Monte Carlo random generation of ash particle ensembles following the statistics of their main descriptive parameters. The minimum significant number of ash parameters, identified for our purposes, is given in Table I and listed as follows: 1) PSD mean equivalent radius r_e; 2) mass concentration C_p; 3) PSD shape parameter μ_p; 4) particle density ρ_p; 5) mean canting angle m_θ of the particle orientation distribution (POD) $p_p(\theta)$; 6) POD canting angle standard deviation σ_θ; 7) axial ratio ρ_{ax}; 8) dielectric constant with an SiO_2 weight W_{SiO2} dependence for the real and imaginary part and relative humidity fraction (RH). **Table I** summarizes the range of values for each parameter, either derived from literature [6], [23], [44] or determined heuristically [1]. Supplementary information, sketched in Table I, are also described in [16].

The lidar backscattering coefficients β_{hh}, β_{vv} and β_{vh} at horizontal (h) and vertical (v) polarization states can be written in terms of the scattering matrix elements S_{xy} and PSD N_p, as:

$$\beta_{xy}(\lambda) = \int_0^\pi \int_0^\infty 4\pi \left|S_{xy}^{(b)}(r,\theta,\lambda)\right|^2 N_p(r) p_p(\theta) dr sin\theta d\theta = \langle 4\pi S_{xy}^{(b)}(r,\theta,\lambda)\rangle \quad (4)$$

where $x=h,v$ again stands for the receiving mode and $y=h,v$ for the transmitting mode polarization. Note that β_{xy} is usually expressed in [$km^{-1}sr^{-1}$]. Considering that β_{xy} can go typically from 10^{-6} up to 10^{-3} $km^{-1}sr^{-1}$, here we prefer to express β_{xy} in dBβ, that is a value in decibel equal to $10\cdot\log_{10}(\beta_{xy})$ when β_{xy} is expressed in [$m^{-1}sr^{-1}$], in analogy to radar meteorology where dBZ is widely used. This means that typical values of backscatter will go from -60 up to -30 dBβ. Note that, for completeness, in **Appendix A** expressions of lidar polarimetric observables are also given in terms of the Stokes vectors and scattering phase (Muller) matrix in order to show the parallelism of definitions for both lidar and radar applications.

The specific attenuation or extinction coefficient α_{xy} is expressed in [km^{-1}] and is defined as:

$$\alpha_{xy}(\lambda) = 2\lambda Im\left\{4\pi S_{xy}^{(b)}(r,\varphi,\lambda)\right\} \quad (5)$$

Similarly to (4), if α_{xy} is in [km^{-1}], $\alpha_{XY}=4.343\cdot\alpha_{xy}$ is conventionally expressed in dB/km. The lidar linear co-polarization and cross-polarization (adimensional) ratio are defined, respectively, by:

$$\delta_{co} = \frac{\beta_{vv}(\lambda) - \beta_{hh}(\lambda)}{\beta_{vv}(\lambda) + \beta_{hh}(\lambda)} \quad (6)$$

$$\delta_{cr} = \frac{\beta_{vh}(\lambda)}{\beta_{hh}(\lambda)} \quad (7)$$

Typically, for a lidar system other parameters are also defined, such as the extinction to backscatter lidar ratio (LR) [sr]:

$$R_{\beta ax}(\lambda) = \frac{\alpha_{xx}(\lambda)}{\beta_{xx}(\lambda)} \quad (8)$$

If the extinction coefficients at two wavelengths λ_1 and λ_2 are known, the extinction Angström coefficient (unitless) can be determined by:

$$A_{ax}\left(\lambda_1/\lambda_2\right) = -\frac{ln[\alpha_{xx}(\lambda_1)\ /\ \alpha_{xx}(\lambda_2)]}{\ln(\frac{\lambda_1}{\lambda_2})} \quad (9)$$

where $\lambda_1 < \lambda_2$. Similarly, we can define the backscatter-related Angström coefficient (unitless) through:

$$A_{\beta x}\left(\lambda_1/\lambda_2\right) = -\frac{ln[\beta_{xx}(\lambda_1)\ /\ \beta_{xx}(\lambda_2)]}{\ln(\frac{\lambda_1}{\lambda_2})} \quad (10)$$

where β_{xx} replaces α_{xx} in (9).

In order to compute the lidar observables in (4)-(10), the non-sphericity of ash particles is considered by assuming spheroids. The particle scattering and absorption properties are computed using the T-matrix method, supplemented by the Geometrical Optics (OG) approach in the optical scattering regime where T-matrix is subject to numerical convergence problems. The T-matrix method has been widely applied to studying non-absorbing and non-spherical particles in the visible and infrared spectral regions [20], [52]. The VALR algorithm can also include the ash-hydrometeor mixed and coexisting classes, in principle, by combining ash and hydrometeor modeling. Hydrometeor

scattering and modeling is well described elsewhere. Any advancement in the understanding of the observed ash clouds can be, in principle, incorporated within the forward model HAPESS in order to generalize its validity and better deal with uncertainty.

For this work, the HAPESS simulations have been limited at the optical wavelength 532 nm. The correlation between the ash concentration C_a and the zenith-pointing visible lidar observables β_{hh}, α_{hh}, δ_{co} and δ_{cr} is shown in **Fig. 1** and **Fig. 2** for each size class VA, FA, CA, SL and LL and all orientations (PO, OO, TO.2 hereinafter called TO and also SP, where SP stands for spherical particle). From these figures we can observe that:

1) the plot of ash class centroids in terms of α_{hh} and α_{hh} clearly shows that LL (the largest size class) exhibits the smallest extinction and backscatter, whereas VA (the smallest size class) the largest. This is related to the scattering properties at 532 nm wavelength LL scatter in deep optical regime, whereas VA follows the Mie scattering resonances.
2) the lidar ratio *LR* is almost constant with respect to co-polar backscatter coefficient β_{hh} for all subclasses, but is sensitive to particle orientation. The lidar ratio LR is more dispersed for prolate and oblate orientation depending on the particle size. These variations are due to microphysical differences of the classes and the predominance of the Mie resonance scattering when the particle size is comparable with the wavelength.
3) the co-polar extinction coefficient α_{hh} is also linearly correlated with C_a for all subclasses and for each frequency. The extinction coefficient highlights a similar behavior of the backscatter coefficient.
4) the co-polarization ratio δ_{co} is not significantly correlated to C_a, but is sensitive to the particle orientation and to the frequency particularly for the size class VA. Indeed, increasing the size class we can observe that the SP particle shows a behavior intercepting other orientation (FA, CA and SL) and mixing for the size class LL.
5) the cross-polarization ratio δ_{cr} is independent from the concentration for all subclasses and varies with TO, PO, OO and SP orientation models and for each frequency, but this behavior is not clear for the VA size class at each considered frequency.
6) the ash mass concentration C_a is almost linearly correlated with co-polar backscatter coefficient β_{hh} for all subclasses and for each frequency. β_{hh} values of LL are larger than those of the VA class since, for a given concentration, in the wavelength-insensitive optical regime the lidar logarithmic response is proportional to the particle concentration number. The latter is smaller for LL particles than for VA particles since, for a given concentration, the volumetric number of big particles is less than that of small particles.

For inversion purposes, it is worth stressing that ash mass concentration and mean equivalent diameter can be derived from a combination of β_{hh} and α_{hh}, whereas δ_{cr} and δ_{co} may be successfully used to better discriminate the ash classes.

B. Retrieval algorithm and parametric models

Several caveats need to be accepted to properly deal with lidar products. The major critical issue is the estimation of the range profile of the extinction coefficient α_{xx}, which can be derived by properly inverting the backscatter profiles in the cloud region where the signal is not totally attenuated and using ad-hoc path attenuation correction algorithms [14], [7]. The latter typically exploits the knowledge of the LR needed to invert the lidar equation after distinguishing the ash from different aerosol contribution [14], [15], [8]. In order to distinguish spherical from non-spherical particles, it is crucial to use a polarimetric lidar instrument [43], [26], [27]. Lidar retrievals are most often based on a solution of the classic lidar equation, which is a single-scattering approximation that ignores higher order multiple scattering. The latter can alter the apparent extinction or transmittance of the medium, produce depolarization of the return signal, and cause a stretching of the return pulse. For most lidar systems the magnitude of the multiply-scattered signal is so small these effects are insignificant and can often be ignored without introducing significant errors, but its impact should be considered in some way [43].

The VALR algorithm allows deriving the main ash particles features from polarimetric lidar observables by means of model-based supervised retrieval algorithm. The algorithm consists of two main steps: ash classification and estimation, both performed in a probabilistic framework using the maximum likelihood (ML) approach. The detection of the ash class from a lidar polarimetric observable set for each range volume can be performed using an ML identification technique. This technique may be considered a special case of the Bayesian approach. Within the latter, the Maximum A posteriori Probability (MAP) criterion can be used to carry out ash cloud classification in a model-based supervised context [19]. The basic rule is to minimize a proper "distance" (or metric) between the measured and simulated polarimetric set, the latter computed by using the microphysical scattering of each ash class, taking into account both the system noise and the a priori available information. If the latter is assumed uniform, MAP becomes the ML method.

The ML technique basically reduces to a minimization process in order to assign the "*c*-th" class to each available lidar measurement. Under the assumption of a) Gaussian likelihood statistics of the difference between simulated and measured observables and b) uncorrelation between the differences (errors) of the same observables, the ML method reduces to the minimization of a quadratic form. The estimated ash class c and the retrieved microphysical parameters are those that exhibit the minimum ML square distance d^2 between the lidar measurement set $\mathbf{x}_m$ and simulated set $\mathbf{x}_s$ of a given class c [16]. If only measurements of attenuation-corrected backscatter coefficient β_{xxmc} and linear cross-polar ratio δ_{crm} are available to define $\mathbf{x}_m$, we can write the following simplified metrics:

$$d^2\left(C_a^{(c)}, D_n^{(c)}\right) = \left[\mathbf{x}_m - \mathbf{x}_s^{(c)}\left(C_a^{(c)}, D_n^{(c)}\right)\right]^T \mathbf{C}_{\varepsilon_x\varepsilon_x}^{-1}\left[\mathbf{x}_m - \mathbf{x}_s^{(c)}\left(C_a^{(c)}, D_n^{(c)}\right)\right] = \frac{\left[\beta_{xxmc} - \beta_{xxs}\left(C_a^{(c)}, D_n^{(c)}\right)\right]^2}{\sigma_{\varepsilon_\beta}^{2\,(c)}} + \frac{\left[\delta_{crm} - \delta_{xxs}\left(C_a^{(c)}, D_n^{(c)}\right)\right]^2}{\sigma_{\varepsilon_\delta}^{2\,(c)}} \quad (11)$$

where "T" stands for the transpose operator, $\mathbf{C}_{\varepsilon_x\varepsilon_x}$ is the autocovariance of the error vector $\boldsymbol{\varepsilon}_x = \mathbf{x}_m - \mathbf{x}_s$ with "-1" its

inverse. In the simplified ML approach with uncorrelated errors, the terms of (11) are basically weighted by the inverse of variances $\sigma^2_{\varepsilon\beta}{}^{(c)}$ and $\sigma^2_{\varepsilon\delta}{}^{(c)}$ of the simulated dataset for the class *c*. In (11) it is explicit that the simulated vector $\mathbf{x}_s$ depends on the unknown C_a and D_n for each class c.

To retrieve the ash parameters such as concentration and mean size within the selected class *c*, we can extract their value from the geophysical parameters whose associated $\mathbf{x}_s$ minimizes the quadratic distance (11) that is:

$$\hat{C}_a^{(c)} = C_a^{(c)} | argmin_{\left(C_a^{(c)}, r_n^{(c)}\right)} \left\{ d^2\left(C_a^{(c)}, D_n^{(c)}\right) \right\} \quad (12a)$$

$$\hat{D}_n^{(c)} = D_n^{(c)} | argmin_{\left(C_a^{(c)}, r_n^{(c)}\right)} \left\{ d^2\left(C_a^{(c)}, D_n^{(c)}\right) \right\} \quad (12b)$$

where *argmin* is the function providing the *minimum* of its argument. It is worth highlighting that these retrievals are conditioned by the numerical forward model accuracy or, in other words, by microphysical-electromagnetic assumptions and their representativeness with respect to the observed scene.

The uncertainty of the ash microphysical estimates in (12), due to noise and the variability of all other geophysical parameters (see Table I), can be derived by taking into account the error statistics around the lidar-based retrieval distance minimum. By assuming an uncertainty of error vector $\boldsymbol{\varepsilon}_x = \mathbf{x}_m - \mathbf{x}_s$ due to instrumental noise and forward model representativeness, we can define an error threshold $\boldsymbol{\delta}_\varepsilon$ associated to this uncertainty (e.g. this threshold $\boldsymbol{\delta}_\varepsilon$ on the backscatter coefficient can be assumed between 10% and 50%, here typically assumed to be 20%). Thus, the standard deviations σ_{Ca} and σ_{Dn} of ash concentration and mean diameter estimates, respectively, are given by:

$$\sigma_{\hat{C}_a}^{(c)} = std\left\{ C_a^{(c)} | d^2\left(C_a^{(c)}, D_n^{(c)}\right) < \delta_\varepsilon^2 \right\} \quad (13a)$$

$$\sigma_{\hat{D}_n}^{(c)} = std\left\{ D_n^{(c)} | d^2\left(C_a^{(c)}, D_n^{(c)}\right) < \delta_\varepsilon^2 \right\} \quad (13b)$$

where *std* is the standard deviation function.

In literature we can find several parametric model allowing to derive the ash concentration from the measured backscatter coefficient. The appealing feature of parametric retrieval techniques is their simplicity in the application to measurements sets, even though the downside is less flexibility (due to the fixed regression model) and frequency scalability (due to the prescribed coefficients valid at a given wavelength).

The first retrieval parametric model (hereinafter PM1), employed to evaluate the ash concentration C_{aPM1} [g/m^3] from ash backscattering, is based on the following relation [27]:

$$C_{aPM1} = k_c \langle R_{\beta\alpha x} \rangle \rho_a \beta_{xxmc} \quad (14)$$

where k_c is the ash conversion factor, function of the particle size distribution. For a large masse k_c is mainly dependent on the ash effective radius r_{ep} (see (1)) and given by $(2/3)\cdot r_{ep}$ [29], [10], [33]. In [22] a value of about 10 μm is assumed for r_{ep} so that k_c is hence set to $0.6\cdot10^{-5}$ m. In (13) $< R_{\beta\alpha x} >$ is the mean value of the estimated lidar ratio [22], [1], [2], ρ_a is the density of volcanic ash fixed to 2450 kg/m^3 [31] and β_{hhm} is the measured volcanic ash backscatter coefficient [39]. The errors on ash mass concentration are evaluated from the uncertainties of $R_{\beta\alpha x}$, β_{hhm} and ρ_a and reach a value of 55%. An additional uncertainty of about 50% must be considered due to the assumption of the effective radius [22], [33]. In absence of other sources, we can derive D_{np} from VALR-ML and assume $r_{ep} = D_{np} / 2$ to estimate k_c in (13).

Another parametric approach, hereinafter referred to PM2, to derive the ash concentration C_{aPM2} [g/m^3] from the measured ash backscatter, [13], [10], can be expressed as:

$$C_{aPM2} = \left[1.346\, r_{ep} - 0.156\right] \langle R_{\beta\alpha x} \rangle \beta_{xxmc} \quad (15)$$

where r_{ep} is the ash effective radius. The expression between square brackets is known as the mass-extinction conversion factor for volcanic ash concentration, depending on the particle effective radius r_{ep} [13], [10]. Indeed, if the information about the effective radius is not available, we can use a simplified version of (14) where the square brackets can be substituted by the mass-extinction conversion factor of 1.45 g/m^2 (95% of the compatible ensembles are in the range 0.87-2.32 g/m^2) [10]. The relative uncertainty of the retrieved mass concentration is estimated to be about 40% and mainly caused by the uncertainty of the microphysics of the particles (size distribution, refractive index and shape) [13]. As in (13), if not available elsewhere, we can derive $r_{ep} = D_{np}/2$ from VALR-ML.

Both parametric PM1 and PM2 models have some a priori information derived from literature or available sources and exploit the correlation between concentration and backscatter. Indeed, by exploiting the HAPESS forward model illustrated in Sect. II.A, we can derive a parametric regressive formula, hereinafter named VALR-Reg, valid at visible wavelengths. A logarithmic relation for estimating ash concentration $C_{aVALR_{Reg}}$ [g/m^3] can be expressed as follows:

$$\hat{C}_{aVALR_{Reg}} = 10^{[a_{VA} + b_{VA}(log_{10}\beta_{xxmc})]} \quad (16)$$

where a_{VA} and b_{VA} (0.8643, 0.8370) are regressive coefficients, derived from HAPESS simulations, including all particle orientations (OO, PO, SP and TO) for very-fine ash VA size class (D_n between 0.125-8 μm).

C Multiple scattering impact

We can attempt to evaluate the uncertainty in the estimated particle extinction due to multiple scattering (MS) within clouds or aerosol layers. If the particle effective radius becomes larger, the probability of multiple scattering increases since a stronger forward scattering causes photons to remain in the field of view of the detector. This MS effect typically leads to an increase of the particle backscatter up to 50% and a consequent underestimation of path attenuation or atmospheric optical depth up to 30% [48]. The MS can affect the lidar measurements, especially in presence of large optical thicknesses. The MS signal increases as the laser beam divergence, the field of view (FOV) of the receiver and the distance between the laser source and the investigated volume increase [47], [48].

Modeling MS effect in lidar response is not an easy task due to path dependence and optical thickness variability. In order to test the sensitivity of backscatter coefficient to the MS, we can simulate its impact on the backscatter coefficient

by introducing an MS factor f_{MS} within the conventional lidar equation. This MS factor f_{MS} is by construction defined between 0 (no MS present) and 1 (full MS). The MS-affected measured backscatter coefficient can be expressed as:

$$\beta_{xxm}^{MS}(s) = \beta_{xxm}(s)e^{2\tau(s)f_{MS}} = \beta_{xxmc}(s)e^{-2\tau(s)}e^{2\tau(s)f_{MS}} = \beta_{xxmc}(s)e^{-2\tau(s)(1-f_{MS})} \quad (17)$$

where s is the range coordinate, τ is the optical thickness (due to the integral of the extinction coefficient α_{xx}) along the two-way path. For simplicity, f_{MS} has been assumed to be range independent, whereas the quantity τ (1- f_{MS}) can be interpreted as the "apparent" optical thickness affected by MS radiation recovery.

In order to evaluate the uncertainty of the ash concentration and mean diameter estimates due to MS effects, we can perform a sensitivity analysis by replacing the measurements lidar dataset (corrected for two-way path attenuation 2τ) with the corresponding quantity $\beta_{xxmc}{}^{MS}$ in (17) where f_{MS} is supposed to be between 0 and 0.3 whereas τ is taken, as a first approximation, from the path-attenuation correction algorithm. This simplified approach does not aim at quantifying the MS effects, but only the sensitivity of the retrievals to its presence. In this respect, we define the total MS standard deviation of C_a and D_n as:

$$\sigma_{C_aMS} = \sqrt{\sigma_{\hat{C}_a}^2 + \sigma_{\hat{C}_af_{MS}}^2} \quad (18a)$$

$$\sigma_{D_nMS} = \sqrt{\sigma_{\hat{D}_n}^2 + \sigma_{\hat{D}_nf_{MS}}^2} \quad (18b)$$

where $\sigma_{\hat{C}_a}^2$,$\sigma_{\hat{D}_n}^2$, $\sigma_{\hat{C}_af_{MS}}^2$, $\sigma_{\hat{D}_nf_{MS}}^2$ are the standard deviations of concentration and mean diameter without and with the MS contribution, respectively.

III. Application To Etna Case Studies

The ML retrieval methodology has been tested on two Etna eruptions: the ash emission of 15 November 2010 and the lava fountain of 12 August 2011. We have applied the VALR-ML to lidar data in order to retrieve the ash concentration and ash particle mean diameter using (12). These retrievals are also compared with those already estimated in [33] and [30] in order to show the VALR-ML potential.

The VAMP scanning lidar system, whose measurement results are used in this work, transmits a linearly polarized laser light at 532nm wavelength and detects parallel and cross-polarized components of the elastic backscattered simultaneously. The VAMP system allows moving in azimuth and elevation with the possibility to scan the volcanic plume either horizontally and/or vertically at a maximum speed of 0.1 rad/s. This system was installed at the "M.G. Fracastoro" astrophysical observatory (14.97° E, 37.69° N), located at 1760 m on the SW flank of the volcano, only 7 km away from the Etna summit craters, allowing the laser beam to scan the atmosphere around the summit craters.

The attenuation-corrected measured backscatter coefficients β_{xxmc} in (10) have been obtained by using the Klett-Fernald algorithm [8], [15]. The LR, as defined in (7), has been assumed to be about 36 sr inside the plume, as described in [22], whereas the contribution of background aerosol load was considered negligible, less than about $10^7 \cdot m^{-1}sr^{-1}$ in the Mediterranean region in clear-sky conditions [36]. Details on the lidar data processing can be found in [22].

To train the VALR-ML algorithm, considering the typical Etna eruption modes and the available observations of distal plumes, we have used a simulated dataset (see sect. II.A and II.B) consisting of the smallest ash class, VA, with orientation classes TO, OO, PO together with a spherical particle class SP. The validity of these a priori choices can be assessed by comparing the measured and simulated observables for both case studies. Note that in the two analyzed study cases, we have selected only the backscatter coefficients correlated to optical depths less than 0.5 and depolarization between 0.1 and 0.5 of ash plume close to lidar system (about 6 km) in order to avoid any possible multiple-scattering influence.

A. Etna ash emission in 2010

The first case study is related to ash emission observed by the VAMP system on 15 November 2010 when both backscatter and depolarization channels were available. During this event, ash emissions from the North East Crater and high degassing from the Bocca Nuova Crater were clearly visible [33]. Water vapor and ash emission occurred every 1-2 min, as reported by volcanologists during a field survey at the summit craters. Different volcanic plume sections were obtained by pointing the laser beam with a fixed direction defined by azimuth angle of 17.3° and three different elevations (14.4°, 14.65° and 14.9°), corresponding approximately to an altitude of 300, 400 and 500 m above summit craters (we will refer to these elevations in terms of corresponding altitudes in the following text) [33].

As mentioned, in order to find the ash size classes best fitting the measured backscatter at the three elevations, we have firstly selected a simulated data subset to train the VALR-ML algorithm. **Fig. 3** shows both measured and simulated ash backscatter and cross-polarization coefficient, expressed in dBβ and in percent, respectively, for VA size class with IC, MC, SC and VC concentrations (see Table I).

Measured lidar observables are fairly well represented and consistent with the simulated ones. In the ash plume layer β_{xxmc} reaches values larger than $2 \cdot 10^{-5}$ $m^{-1} \cdot sr^{-1}$ (-47 dBβ) with the highest values of about $5 \cdot 10^{-5}$ $m^{-1} \cdot sr^{-1}$ (-43 dBβ), usually associated to a larger concentration of volcanic aerosols [32]. In all cases the average and maximum linear cross-polarization is about 4-6% and 24-26%, respectively. The latter values are a clear indication of a complex morphology of ash particles, the relatively high cross-polarization being a significant indicator of non-sphericity [42].

It is worth remembering that the uncertainty of δ_{crm} comes primarily from systematic errors in the setup of the lidar systems, which cannot be reduced by statistical methods. Indeed, we have found that the main error sources originate from the depolarization calibration (with large differences between the different calibration methods) and by backscatter coefficient correction due to the uncertainty in the height-dependent lidar ratio and the uncertainty in the signal calibration in the assumed clean and free troposphere [9]. High particle depolarization values of about 30-35 % are observed in the main volcanic ash layer and are similar to

those found elsewhere with values of 35-38 % [2], [5] [24]. The latter values suggest a large fraction of volcanic aerosols. Low values of δ_{crm} and values between 1% < δ_{crm} < 2% are typically associated to spherical particles [13].

Fig. 4 shows, for each considered elevation (labeled with respect to height in meters above the crater), the measured backscatter coefficient, again expressed as dBβ, and the volumetric depolarization ratio. The latter presents a variability between 2% and 25%, whereas few pixels show higher values. By applying the VALR-ML algorithm to data of Fig. 4, **Fig. 5** shows the ash concentration and mean diameter retrievals, considering both measured lidar observables β_{xxmc} and δ_{crm} and only the backscatter coefficient β_{xxmc}. The latter indicates that, at each elevation angle and when we consider both the measured lidar observables, the average concentration is about 8.63 ± 6.04 mg/m^3 and the mean diameter is about 3.37 ± 2.04 μm. If only the backscatter coefficient is taken into account, the average concentration is about 13.01 ± 4.50 mg/m^3 and the mean diameter about 5.80 ± 2.46 μm. This means that, using only backscatter measurements, the retrieved values are on average larger than about 66% and 58% for concentration and mean diameter, respectively, with respect to the 2-observable setup. A more complete set of lidar observables (two or more) tends to preserve the smaller sizes and concentrations with a larger variability (standard deviation) of both ash concentration and mean diameter. Note also that VALR-ML retrieval results suggest that the availability of depolarization measurements: 1) provides a more likely retrieval of non-spherical particles with a given shape/orientation; 2) has a positive impact on the class discrimination.

The standard deviation $\sigma_{\hat{C}_a}$ and $\sigma_{\widehat{D}_n}$ of the lidar-based VALR-ML retrievals can be estimated using (13) for both ash concentration and mean diameter, respectively. As mentioned in sect. II.C, the impact of multiple scattering can be at least evaluated in terms of increased uncertainty $\sigma_{\hat{C}_a f_{MS}}$ and $\sigma_{\widehat{D}_n f_{MS}}$ of the lidar-based retrievals, playing with the multiple scattering factor f_{MS} defined in (17). In this respect, block *a*) of **Table II** shows the uncertainties as percentage ratio of the averaged standard deviation $< \sigma_{\hat{C}_a} >$ (without multiple scattering effects) and $< \sigma_{\hat{C}_a f_{MS}} >$ (with multiple scattering effects) with respect to the average $< \hat{C}_a >$ as well as the percentage ratio for the estimate of the mean diameter $\widehat{D}_n$. Note that the average values are computed over all the performed retrievals and are needed to introduce an overall score. Results of Table II indicate that on average both ash concentration and mean diameter retrievals are not very sensitive to multiple scattering effects (e.g. concentration estimate uncertainty goes from about 40% up to 43%, whereas the mean diameter one from 4% up to 7%). Indeed, mean dimeter estimates seem to be more affected by the increase of the multiple scattering fraction f_{MS}. This is not surprising since, as already mentioned, we have properly selected only measurements close to the lidar system (about 6 km) in order to limit any possible multiple-scattering influence.

B. Etna lava fountain in 2011

The second test case analyzed here, is related to the Etna lava fountain of 12 August 2011, when both backscatter and depolarization channel were available. The scanning by the VAMP system was performed by changing the elevation angle between 20° and 59° with a fixed azimuth of 36.7°. Lidar measurements were acquired from 08:59 till 11:56 UTC. The volcanic particles were observed between 6.5 km and 8.0 km from the lidar station along the laser beam path, when a column height of about 7 km above sea level was present, as shown by the cross section of the corrected backscatter coefficient in **Fig. 6** [30].

We have used the same simulated training dataset, previously discussed in Sect. II.A, obtaining the most likely ash size classes similar to those on 15 November 2010 but with a larger ash concentration (about one order of magnitude), as shown in the second panel in Fig. 6. The latter is derived from the PM1 algorithm showing a mean concentration of about 9 mg/m^3.

The VALR-ML derived ash concentration and mean diameter are shown in **Fig. 7**, considering a training dataset with (complete) and without (partial) spherical particles (SPs). In both cases, the average concentration is about 65.00 ± 37.3 mg/m^3 and the mean diameter is about 3.01 ± 1.2 μm as shown in **Table III**, which also includes the sensitivity analysis due to the inclusion or exclusion of spherical particles within the training dataset. The percentage ratio between the number of spherical classes and the number of total detected ash classes is about 37%. This ratio underlines the impact of volumetric depolarization measurements useful to distinguish the ash particle category. It is remarkable how the lack of depolarization observables does not significantly affect the retrievals of ash size and concentration.

Note that for this case study an independent estimate, based on ground measurements and forecast model simulations, of the ash particle size distribution is available in terms of percentage weight [30]. The latter is obtained using the Lagrangian numerical PUFF model ([34], [38]) inside the region investigated by lidar [30]. The measured size distribution is clearly asymmetric, well approximated by a log-normal or a Gamma distribution [30]. The PUFF-based average ash particle size is about 5.3 μm, slightly larger than VALR-ML based mean diameter retrieval (3.01 ± 1.22 μm).

Fig. 8 shows the range profiles of the measured backscattering coefficient and depolarization ratio, obtained by pointing the VAMP laser beam toward the plume for 10 min (09:01–09:11 UTC) and when the eruption column reached the height of 9 ± 0.5 km. Lidar profiles show two layers with different properties. The first ash layer, at 6.1 km from the lidar station along the laser beam, is characterized by lower β_{xxmc} of about -58 dBβ and δ_{crm} of about 5%. The second ash layer, located between 6.2 and 6.8 km, is characterized by high peak values of β_{xxmc} of about -41 dBβ and δ_{crm} of about 20%, suggesting that volcanic ash was mainly contained in this layer [30].

The VALR-ML retrievals in terms of concentration and mean diameter are also shown in the lower panels of Fig. 8. The ash concentration peak is about 100 mg/m^3, whereas the mean diameter reaches a maximum value of 6.3 μm. In order to attribute an uncertainty to VALR estimations, we have assumed a backscattering coefficient error of 50% so that the standard deviation of both ash concentration and mean diameter are evaluated and associated to each estimate, as in (12). This uncertainty is shown in Fig. 8. Note that there are ranges in Fig. 8 where, for a higher backscatter, we can

retrieve a lower concentration from VALR-ML. This may seem a contradiction, but looking at (3) we realize that the same β_{xxmc} can be associated to a large concentration of small particles or, vice-versa, to a small concentration of large particles. Thus the simultaneous retrieval of both C_a and D_n is essential to interpret this ambiguity.

The impact of multiple scattering in this case study shows the same behavior of the previously analyzed case, as shown in blocks *b*) and *c*) of Table II. Indeed, the uncertainty, expressed as a percentage ratio, highlights how a smaller variability of ash concentration and mean diameter is associated to an increase of f_{MS}, especially for higher altitudes.

C. Comparison with parametric model retrievals

There is a reasonable interest in comparing the VALR-ML technique with other parametric methods in order to understand the potential of a physically-based approach with respect to more straightforward parametric procedures.

The HAPESS forward model simulations at 532 nm can provide an effective way to compare the 3 parametric retrieval approaches (13), (14), (15) together with VALR-ML. **Fig. 9** shows the HAPESS simulations superimposed on results of the selected models PM1 in (13) (assuming LR=36 sr and $r_{eff} = < D_n > / 2$ from the considered size class) and PM2 in (14) (assuming a default mass-extinction conversion factor of 1.45 g/m^2 and $r_{eff} = < D_n > / 2$ from the considered size class) together with VALR-Reg in (15). The PM1 formula for all orientations shows a higher ash concentration, whereas the PM2 typically lies between PM1 and VALR-Reg (which is the best approximation of HAPESS simulated data by definition). For the same backscatter coefficient, the VALR-Reg model tends to predict a larger ash concentration. Indeed, VALR-ML estimates may be larger or smaller than VALR-Reg as the forward model simulations are randomly distributed around the regression curve. This is due to the inherent best-fitting approach of the VALR-Reg model (and any other regressive approach) that is based on a minimization of the simulated points with respect to the modeled regression curve.

A first example of intercomparison is shown in **Fig. 10** where the profile of Fig. 8, related to 12 August 2011 lidar data, is reconsidered. In the first panel the HAPESS simulations and the few measured samples are superimposed. The second panel highlights the estimates of three analyzed parametric models compared with the VALR-ML one, already shown in Fig. 8. The PM1 parameters in (13) are similar to those in Fig. 9, but r_{eff}=10 μm as assumed in [30], whereas PM2 is applied without modifications. PM1 estimates, in this set up, are not always larger than the others, whereas VALR-ML ones are typically but not necessarily lower, being PM2 and VALR-Reg in the bottom.

A second application of the parametric retrieval models is shown in **Fig. 11** for the event of Etna eruption on 15 November 2010. This figure is, indeed, the output of a sensitivity study as it plots both retrievals from PM1 in (13) using $r_{eff} = D_n/2$ derived from VALR-ML and PM1 with a fixed value $r_{eff} = 10\ \mu m$ as assumed in [30]. As expected, VALR-ML based ash concentration retrievals are partly lower than those of PM1 due to the difference in the average particle size. This points out the impact of an arbitrary assumption of the effective ash radius on ash retrievals.

The lidar data analysis may help quantifying the impact that ash emissions may have on aviation safety in order to prevent flights in areas of high ash contamination whose lower threshold is $2\cdot10^{-4}$ g/m^3 in compliance with the International Civil Aviation Organization (ICAO) directives. In this respect, besides $2\cdot10^{-4}$ g/m^3, we can define four concentration ranges using increasing ash concentration values equal to $2\cdot10^{-3}$ g/m^3, $3\cdot10^{-3}$g/m^3 and $4\cdot10^{-3}$ g/m^3. Using these thresholds, we can identify 4 areas: LOWER (less than $2\cdot10^{-4}$ g/m^3), LOW (between $2\cdot10^{-4}$ g/m^3 and $2\cdot10^{-3}$ g/m^3), MEDIUM (between $2\cdot10^{-3}$ g/m^3 and $4\cdot10^{-3}$ g/m^3) and HIGH (larger than $4\cdot10^{-3}$ g/m^3).

Results are shown in **Fig. 12** in terms of spatial maps for the 15 November 2010 Etna eruption. These panels refer to elevations corresponding to altitudes of 300, 400 and 500 m, respectively (see Fig. 4) and shows only the ash concentration maps retrieved from VALR-ML and PM1 (set up as in Fig. 11 which as a standard configuration [30]). As expected, for each elevation, VALR-ML ash concentration retrievals are generally lower than those derived from PM1. Indeed, a smaller amount of pixels are labelled as LOW and a larger quantity as HIGH by VALR-ML, whereas most pixels are classified as HIGH and MEDIUM by PM1 model, coherently with the previous retrievals and discussion (see Figure 8).

Even though no validation dataset is available to assess the overestimation of parametric models, it can be interesting to quantitatively evaluate the impact of lidar-based retrievals in terms of no flight zones. To this end, we have computed these differences in terms of weighted occurrences with respect to three concentration thresholds ($Th_1 = 2\cdot10^{-4}$ g/m^3, $Th_2 = 2\cdot10^{-3}$ g/m^3 and $Th_3 = 4\cdot10^{-3}$ g/m^3) following the ICAO regulations, as shown in the **Table IV**. Substantially, if both techniques are above the given threshold there is a HIT, if PM1 is below and VALR-ML is below there is NEG, if PM1 is above and VALR-ML is below there is a FALSE, if PM1 is below and VALR-ML is above there is a MISS. From Table IV it emerges that, as expected, considering less restrictive ash thresholds the HIT cases tend to decrease, the NEG and MISS cases tend to increase linearly, whereas FALSE cases grow, but for the Th_2 larger values are noted essentially due to the PM1 estimates around this Th_2 value ($2\cdot10^{-3}$ g/m^3).

IV. CONCLUSIONS

The use of a scanning lidar located near volcanic sites may be useful to monitor volcanic activity and help drastically reduce the risks to aviation during these eruptions. The application of the VALR-ML algorithm to lidar data allows estimating ash concentration and size class in a physically-consistent framework in order to better understand the eruptive activity nature. The analyzed Etna cases, using the scanning lidar system at visible wavelength, show that this sensor can be employed to detect the lowest ash concentration values of dispersed plumes in the atmosphere.

The proposed VALR-ML methodology can help finding the main microphysical ash features and the areas characterized by a specific mass concentration of smallest ash particles. This information may help quantify the impact that ash emissions have on aviation safety to halt flights in areas of high ash contamination (where the threshold is typically set to $2\cdot10^{-3}$ g/m^3) in compliance with the ICAO. In

the considered case study, the flight-interdicted area has been extended when using the proposed VALR-ML due to lower estimates of ash concentrations. Moreover, the knowledge of reliable ash concentration in the atmosphere may help better define the main eruption source parameters within ash dispersal models, thus improving our ability to forecast volcanic ash cloud aerial distribution.

The impact of using an advanced retrieval algorithm, such as VALR-ML, with respect to parametric retrieval techniques, has an appealing potential for improving ash mass concentration retrievals. The VALR-ML approach allows to perform a more accurate ash concentration retrieval using several lidar observables. If several lidar observables are not available, the VALR-Reg model represents a physically-based efficient compromise. Future work shall be devoted to assess the results presented in this work by selecting more case studies where other lidar data are collected or performing new measurements with the aim of testing the model.

APPENDIX A. FROM SCATTERING MATRIX TO MUELLER MATRIX AND LIDAR OBSERVABLES.

Electromagnetic scattering simulations can be performed in two basic and mutually related coordinate systems: the *Forward Scatter Alignment* (FSA) convention and the *Back Scatter Alignment* (BSA) convention [21], [51]. Given an incident field upon the target, in the FSA system, the scattered far-field is basically an outward wave from the target, whereas in the BSA system, it is a backward wave incident upon the target itself (useful for monostatic systems). The polarimetric response of a point or distributed target can be obtained by simultaneously measuring both the amplitude and phase of the scattered field using two orthogonal channels [26]. If the incident and scattered field vectors are decomposed into their horizontal (parallel) and vertical (orthogonal) components:

$$\boldsymbol{E}^i = \boldsymbol{E}^i_v \hat{v}_i + \boldsymbol{E}^i_h \hat{h}_i \quad \text{(A.1)}$$

$$\boldsymbol{E}^s = \boldsymbol{E}^s_v \hat{v}_s + \boldsymbol{E}^s_h \hat{h}_s \quad \text{(A.2)}$$

the polarimetric response can be represented by the scattering matrix $\boldsymbol{S}$, which for plane wave illumination is given by [41]:

$$\boldsymbol{E}^s = \frac{e^{jkr}}{r}\begin{bmatrix} S_{vv} & S_{vh} \\ S_{hv} & S_{hh} \end{bmatrix}_{FSA} \boldsymbol{E}^i = \mathbf{S}_{\mathrm{FSA}} \boldsymbol{E}^i \quad \text{(A.3)}$$

where r is the distance from the sensor to the center of the distributed target and S_{pq} are called the scattering amplitudes in the FSA convention with $\mathbf{S}_{\mathrm{FSA}}$ the complex scattering matrix. In the backscattering case, reciprocity implies that $S_{vh} = S_{hv}$. Each complex element of the scattering matrix can be represented by [26]:

$$S_{pq} = |S_{pq}| e^{j\phi_{pq}} = \sum_{n=1}^{N} |S^n_{pq}| \, e^{i\phi^n_{pq}} \quad \text{(A.4)}$$

with $p,q=h,v$ and where N is the total number of scatters that constitute the distributed target, each having scattering amplitude $|S^n_{pq}|$ and phase ϕ^n_{pq}. It is possible to use a more efficient approach to represent the relationship between the scattered and incident field, based on the Stokes vector. Indeed, each complex scattering matrix (2 x 2) is converted to their corresponding real Mueller matrix or Stokes scattering operators (4 x 4). The elements of the Stokes vector are defined as:

$$\boldsymbol{I} = \begin{cases} I = |E^i_h|^2 + |E^i_v|^2 \\ Q = |E^i_h|^2 - |E^i_v|^2 \\ U = -2Re(E^{i*}_h E^i_v) \\ V = 2Im(E^{i*}_h E^i_v) \end{cases} \quad \text{(A.5)}$$

Physically **I** is proportional to the total power, whereas Q, U and V contain the information about the polarization state. The *modified* Stokes vector representation of a polarized wave can also be introduced by defining $I_v = I + Q$ and $I_h = I - Q$ instead of I and Q, respectively.

The relationship between transmitted and scattered Stokes vectors is expressed as a function of ensemble-average Mueller scattering matrix $\mathbf{M}_{\mathrm{FSA}}$ (in m^2) and decreases as $1/r^2$ for a mixture of particles [41], [28]:

$$\boldsymbol{I}^s = \frac{1}{r^2}\mathbf{M}_{\mathrm{FSA}}\boldsymbol{I}^i \quad \text{(A.6)}$$

A further useful definition is the normalized ensemble-average Mueller scattering matrix $\widetilde{\boldsymbol{M}}$ or scattering phase matrix:

$$\widetilde{\boldsymbol{M}} = \frac{4\pi}{k_s}\mathbf{M}_{\mathrm{FSA}} \quad \text{(A.7)}$$

where all elements are averaged over the size distribution and orientation of the particle polydispersion, as shown in (3). For example, it holds:

$$M_{11} = < \frac{1}{2}(|S_{hh}|^2 + |S_{hv}|^2 + |S_{vh}|^2 + |S_{vv}|^2) >$$

$$M_{22} = < \frac{1}{2}(|S_{hh}|^2 - |S_{hv}|^2 - |S_{vh}|^2 + |S_{vv}|^2) >$$

with the angle brackets standing for the ensemble average. The elements of the ensemble-average Mueller matrix $\mathbf{M}_{\mathrm{FSA}}$ are quantities given in terms of the elements of the scattering matrix $\mathbf{S}_{\mathrm{FSA}}$:

It is noted that the reciprocity relation, which is a manifestation of the symmetry of the scattering process with respect to an inversion of time [28], satisfies the condition $S_{hv} = S_{vh}$ in FSA convention and $S_{hv} = -S_{vh}$ in BSA. The Mueller matrix of a distributed target of partially oriented particles, for which S_{hv} is uncorrelated with S_{vv} and S_{hh} contains only eight non-zero elements [41]:

$$\mathbf{M}_{\mathrm{FSA}} = \begin{bmatrix} M_{11} & M_{12} & 0 & 0 \\ M_{21} & M_{22} & 0 & 0 \\ 0 & 0 & M_{33} & M_{34} \\ 0 & 0 & M_{43} & M_{44} \end{bmatrix} \quad \text{(A.8)}$$

For randomly oriented particles, the scattering medium is macroscopically isotropic and mirror-symmetric with respect to any plane, and in backward direction ($\theta = 180°$). This implies the following conditions in (A.8):

$$M_{44}(180°) = M_{11}(180°) - 2M_{22}(180°)$$

$$M_{33}(180°) = -M_{22}(180°)$$

$$M_{12}(180°) = M_{21}(180°) = M_{34}(180°) = 0$$

For elastic lidar applications, it is usual to define the backscattering coefficients (in km^{-1} sr^{-1}), co-polar and cross-polar, defined as combination of the elements of $\mathbf{M}_{\mathrm{FSA}}$ as (e.g., [24], [10], [26]):

$$\begin{aligned}\beta_{hh} &= < 4\pi|S_{hh}|^2 > = < \frac{2\pi(M_{11} - M_{12} - M_{21} + M_{22})}{10^3} > \\ \beta_{vv} &= < 4\pi|S_{vv}|^2 > = < \frac{2\pi(M_{11} + M_{12} + M_{21} + M_{22})}{10^3} > \\ \beta_{hv} &= < 4\pi|S_{hv}|^2 > = < \frac{2\pi(M_{11} + M_{12} - M_{21} - M_{22})}{10^3} >\end{aligned} \quad (A.9)$$

The lidar linear cross-polarization ratio and co-polarization are defined, respectively, as:

$$\begin{aligned}\delta_{cr} &= \frac{\beta_{hv}}{\beta_{hh}} = \frac{< M_{11} + M_{12} - M_{21} - M_{22} >}{< M_{11} - M_{12} - M_{21} + M_{22} >} \\ \delta_{co} &= \frac{\beta_{vv} - \beta_{hh}}{\beta_{vv} + \beta_{hh}} = \frac{< M_{12} + M_{21} >}{< M_{11} + M_{22} >}\end{aligned} \quad (A.10)$$

It is noted that in the case of randomly oriented particles $M_{12} = M_{21} = 0$ so that the expression of δ_{cr} is equal to the ratio of the copolar elements only of the Mueller matrix, as shown in (5) and (6). The lidar ratio, defined in (7), is expressed as a function of the single-scattering albedo w_0 and M_{11}:

$$R_{\beta\alpha} = \frac{w_0 M_{11}}{4\pi} \quad (A.11)$$

where

$$w_0 = \frac{k_s}{k_e} = \frac{M_{11}}{k_e} \quad (A.12)$$

being k_s and k_e the scattering and extinction coefficients (in km^{-1}), respectively, of the particle ensemble, the latter expressed by the extinction theorem:

$$k_e = \frac{4\pi}{k_0} \langle Im\{M_{11}\} + Im\{M_{22}\} \rangle$$

Note that, in analogy to lidar, for radar applications several similar observables can be defined such as the radar volumetric co-polar reflectivity (in $m^2 \cdot m^{-3}$) at horizontal and vertical polarizations [51]:

$$\begin{aligned}\eta_{hh} &= \langle 4\pi \frac{1}{2}(M_{11} - M_{12} - M_{21} + M_{22}) \rangle \\ \eta_{vv} &= \langle 4\pi \frac{1}{2}(M_{11} + M_{12} + M_{21} + M_{22}) \rangle\end{aligned} \quad (A.13)$$

where the elements of the Mueller matrix are, indeed, typically expressed in BSA convention. The volumetric cross-polar reflectivity (in $m^2 \cdot m^{-3}$) is defined as,

$$\eta_{hv} = \langle 4\pi \frac{1}{2}(M_{11} + M_{12} - M_{21} - M_{22}) \rangle \quad (A.14)$$

The radar reflectivity factor (in dBZ if the reflectivity is in $mm^6 \cdot m^{-3}$) is defined as:

$$Z_{xy} = 10log_{10} \frac{\lambda^2 2\pi}{\pi^5 |K_p|^2} \eta_{xy} \quad (A.15)$$

where K_p is a dielectric factor and η_{xy} is expressed in $mm^6 \cdot m^{-3}$. The differential reflectivity (in dB) and linear depolarization ratio (in dB) can also be defined as:

$$\begin{aligned}Z_{dr} &= 10log_{10} \frac{\eta_{hh}}{\eta_{vv}} \\ L_{dr} &= 10log_{10} \frac{\eta_{vh}}{\eta_{hh}}\end{aligned} \quad (A.16)$$

ACKNOWLEDGMENT

This work has been partially supported by the European FP7 project APHORISM (FP7 – SPA - 2013, n. 606738) and by H2020 project EUROVOLC (Proposal n. 731070-2, call H2020-INFRAIA-2017-1).

REFERENCES

[1] Armienti, P., G. Macedonio, and M. T. Pareschi, 1988: A numerical model for simulation of tephra transport and deposition: Applications to May 18, 1980, Mount St. Helens eruption. J. Geophys. Res., 93 (B6), 6463–6476.

[2] Ansmann A, Tesche M, Seifert P, Groß S, Freudenthaler V, Apituley A, Wilson KM, Serikov I, Linné H, Heinold B, Hiebsch A, Schnell F, Schmidt J, Mattis I, Wandinger U, Wiegner M, "Ash and fine–mode particle mass profiles from EARLINET–AERONET observations over central Europe after the eruptions of the Eyjafjallajökull volcano in 2010", J. Geophys Res 116: D00U02; Doi: 10.1029/2010JD015567, 2011.

[3] Ball J. G. C., Reed B. E., Grainger R. G., Peters D. M., Mather T. A. and Pyle D. M., "Measurements of the complex refractive index of volcanic ash at 450, 546.7, and 650 nm", J. Geo-phys. Res. Atmos., 120, 7747-7757, doi: 10.1002/2015JD023521, 2015.

[4] Casedevall J. T., "Volcanic ash and aviation safety: proceeding of the first international Symposium on volcanic ash and aviation safety", U.S. Geological Survey Bulletin, pp. 2047, 1994.

[5] Chazette, P., Bocquet, M., Royer, P., Winiarek, V., Raut, J.- C., Labazuy, P., Gouhier, M., Lardier, M., and Cariou, J.-P., "Eyjafjallajkull ash concentrations derived from both lidar and modeling", J. Geophys. Res.-Atmos., 117, D00U14, doi:10.1029/2011JD015755, 2012.

[6] Coltelli M., Miraglia L., and Scollo S., "Characterization of shape and terminal velocity of tephra particles erupted during the 2002 eruption of Etna volcano, Italy," *Bull. Volcanol.*, vol. 70, no. 9, pp. 1103–1112, doi: 10.1007/s00445-007-0192-8, 2008.

[7] Ferguson, J. A., and Stephens, D. H. "Algorithm for inverting lidar returns". Appl. Opt. , 22, 3673-3675, 1983.

[8] Fernald, F.G., "Analysis of atmospheric lidar observations: Some comments", Appl. Optic. , 23, 652–653, 1984.

[9] Freudenthaler V., Esselborn M., Wiegner M., Heese B., Tesche M., Ansmann A., Müller D., Althausen D., Wirth M., Fix A., Ehret G., Knippertz P., Toledano C., Gasteiger J., Garhammer M. and Seefeldner M., "Depolarization ratio profiling at several wavelengths in pure Saharan dust during SAMUM 2006", Tellus 61B, 165–179, 2009.

[10] Gasteiger J, Groß S, Freudenthaler V, Wiegner M, Volcanic ash from Iceland over Munich: mass concentration retrieved from ground-based remote sensing measurements. Atmos Chem Phys 11:2209–2223, 2011.

[11] Gertiser, R., Self, S., Gaspar, J., Kelley, S.P., Pimental, A., Eikenberg, J., Barry, T., Pacheco, J., Queiroz, G., Vespa, M., "Ignimbrite stratigraphy and chronology on Terceira Island, Azores". In: Gropelli, G., Viereck-Goette, L. (Eds.), Stratigraphy and Geology of Volcanic Areas: Geological S. America Special paper, 464, pp. 133–154, 2010.

[12] Gobbi, G. P., F. Congeduti, and A. Adriani, 1992: Early stratospheric effects of the Pinatubo eruption. Geophys. Res. Lett., 19, 997–1000.

[13] Gross S., Freudenthaler V., Wiegner M., Gasteiger J., Geiß A., Schnell F., "Dual-wavelength linear depolarization ratio of volcanic aerosols: Lidar measurements of the Eyjafjallajökull plume over Maisach, Germany", Atmospheric Environment 48 (2012) 85-96, doi: 10.1016 / j.atmosenv. 2011.06.017, 2012.

[14] Klett, J.D., " Stable Inalytical inversion solution for processing lidar returns", Appl. Opt. 20, 211e220, 1981.

[15] Klett, J.D. " Lidar inversion with variable backscatter/extinction ratios", Appl. Optics, 24, 1638–643, 1985.

[16] Marzano F. S., L. Mereu, M. Montopoli, D. Cimini AND G. Martucci, "Volcanic Ash Cloud Observation using Ground-based Ka-band Radar and Near-Infrared Lidar Ceilometer during the Eyjafjallajökull eruption", *Annals of Geophysics*, Fast Track 2, 2014.

[17] Marzano F. S., E. Picciotti, G. Vulpiani, and M. Montopoli, "Synthetic signatures of volcanic ash cloud particles from X-band dual-polarization radar," IEEE Trans. Geosci. Remote Sens., vol. 50, no. 1, pp. 193–211, Jan. 2011.

[18] Mather, T. A., D. M. Pyle, and C. Oppenheimer, "Tropospheric volcanic aerosol. Volcanism and the Earth's Atmosphere", Geophys. Monogr., Vol. 139, Amer. Geophys. Union, 189–212, 2003.

[19] Mereu L., Marzano F.S., Montopoli M. and Bonadonna C., "Exploiting microwave scanning radar fro monitoring Icelandic volcanic eruption source parameters", European Radar Conference (EuRAD), 2014 11th, Doi: 10.1109/ EuRAD.2014.6991243, 2014.

[20] Mishchenko I. M., Travis L. D., "T-matrix computations of light scattering by large spheroidal particles", Optics Comm., 109, 16-21, 1994.

[21] Pieri D., C. Ma, J. J. Simpson, G. Hufford, T. Grindle, and C. Grove, "Analyses of in-situ airborne volcanic ash from the February 2000 eruption of Hekla Volcano, Iceland," Geophys. Res. Lett. , vol. 29, no. 16, pp. 1767–1770, 2002.

[22] Pisani, G., A. Boselli, M. Coltelli, G. Leto, G. Pica, S. Scollo, N. Spinelli, and X. Wang , "Lidar depolarization measurement of fresh volcanic ash from Mt. Etna, Italy", Atmos. Environ. , 62, 34–40, 2012.

[23] Riley C. M., Rose W. I., and Bluth G. J. S., "Quantitative shape measurements of distal volcanic ash," *J. Geophys. Res.*, vol. 108, no. B10, pp. 2504–2514, 2003.

[24] Rolf C., Kramer M., Schiller C., Hildebrandt M. and Riese M., "Lidar observation and model simulation of a volcanic-ash-induced cirrus cloud during the Eyjafjallajokull eruption", Atmos. Chem. Phys., 12, 10281–10294, 2012, doi:10.5194/acp-12-10281-2012.

[25] Rose, W.I., Durant, A.J., Fine ash content of explosive eruptions, Journal of Volcanology and Geothermal Research (2009), doi:10.1016/j.jvolgeores.2009.01.010

[26] Sassen K, Polarization in lidar. In: Weitkamp C (ed) Lidar. Springer, New York, pp 19–42, 2005.

[27] Sassen K, Zhu J, Webley P, Dean K, Cobb P, Volcanic ash plume identification using polarization lidar: Augustine eruption, Alaska. Geophys Res Lett 34. Doi: 10.1029/2006GL027237, 2007.

[28] Saxon D. S., "Tensor Scattering Matrix for electromagnetci field", Phys. Rev. 100, 1771-1775, 1995.

[29] Schumann U, Weinzierl B, Reitebuch O, Schlager H, Minikin A, Forster C, Baumann R, Sailer T, Graf K, Mannstein H, Voigt C, Rahm S, Simmet R, Scheibe M, Lichtenstern M, Stock P, Rüba H, Schäuble D, Tafferner A, Rautenhaus M, Gerz T, Ziereis H, Krautstrunk M, Mallaun C, Gayet JF, Lieke K, Kandler K, Ebert M, Weinbruch S, Stohl A, Gasteiger J, Groß S, Freudenthale V, Wiegner M, Ansmann A, Tesche M, Olafsson H, Sturm K, "Airborne observations of the Eyjafjalla volcano ash cloud over Europe during air space closure in April and May 2010". Atmos Chem Phys 11:2245–2279, 2011.

[30] Scollo S., A. Boselli, M. Coltelli, G. Leto, G. Pisani, M. Prestifilippo, N. Spinelli and X. Wang, "Volcanic ash concentration during the 12 August 2011 Etna eruption", Geophys. Res. Lett. , 42, doi: 10.1002/2015-GL063027, 2015.

[31] Scollo S, Coltelli M, Prodi F, Folegani S, Natali S, "Terminal settling velocity measurements of volcanic ash during the 2002– 2003 Etna eruption by an X-band microwave raingauge disdrometer. Geophys Res Lett 32. doi:10.1029/2004-GL022100, 2005.

[32] Scollo S., M. Prestifilippo, G. Spata, M. D'Agostino, and M. Coltelli, "Monitoring and forecasting Etna volcanic plume", Nat. Hazards Earth Syst. Sci., 9, 1573–1585, 2009.

[33] Scollo, S., A. Boselli, M. Coltelli, G. Leto, G. Pisani, N. Spinelli, and X. Wang, " Monitoring Etna volcanic plumes using a scanning lidar, Bull. Volcanol., 74, 2382–2395, doi:10.1007/s00445-012-0669-y, 2012.

[34] Searcy, C., K. Dean, and W. Stringer, "PUFF: A high-resolution volcanic ash tracking model, J. Volcanol. Geotherm. Res., 80, 1–16, 1998.

[35] Shettle E.P:, Fenn R.W.,"Models for the Aerosol of the Lower Atmospere and the Effect of Humidity Variation on their Optical Properties. Environmental research papers, no.076, 1979.

[36] Sicard M, Guerrero-Rascado JL, Navas-Guzman F, Preissler J, Molero F, Tomas S, Bravo-Aranda JA, Comeron A, Rocadenbosch F, Wagner F, Pujadas M, Alados-Arboledas L, "Monitoring of the Eyjafjallajokull volcanic aerosol plume over the Iberian Peninsula by means of four EARLINET lidar stations. Atmos Chem Phys 12:3115–3130, 2012.

[37] Sparks R.S.J., Bursik M. I. , Carey S.N., Gilbert J.S., Glaze L. S. ,Siggurdsson H. and Woods A.W. 1997): Volcanic Plumes (John Wiley and Sons, New York), pp. 574.

[38] Tanaka, H. L., and K. Yamamoto, "Numerical simulation of volcanic plume dispersal from Usu Volcano in Japan on 31 March 2000 using PUFF model", Earth Planets Space, 54, 743–752, 2002.

[39] Tesche M, Ansmann A, Muller D, Althausen D, Engelmann R, Freudenthaler V, Groβ S, "Separation of dust and smoke profiles over Cape Verde by using multi-wavelength Raman and polarization lidars during SAMUM 2008". J Geophys Res 114: D13203. Doi: 10.1029/2009JD011862, 2009.

[40] Tesche M., Ansmann A., Müller D., Althausen D., Engelmann R., Freudenthaler V., Groß S., "Vertically resolved separation of dust and smoke over Cape Verde using multiwavelength Raman and polarization lidars during Saharan Mineral Dust Experiment 2008". J. Geophys. Res., vol. 114. doi:10.1029/2009JD011862, 2009.

[41] Ulabi F. T., Sarabandi K., Nashashibi A., "Statistical properties of the Mueller Matrix of distributed targets", IEE Procedings-F. Vol. 139, No. 2, April 1992.

[42] Wiegner M., Gasteiger J., Groß S., Schnell F., Freudenthaler V., Forkel R., "Characterization of the Eyjafjallajökull ash-plume: Potential of lidar remote sensing", Physics and Chemistry of the Earth, 45–46, 79–86, 2012.

[43] Winker D. M., Osborn MT, "Preliminary analysis of observations of the Pinatubo volcanic plume with a polarization-sensitive lidar". Geophys Res Lett, 19:171–174, 1992.

[44] Wohletz K. H., Sheridan M. F., and Brown W. K., "Particle size distributions and the sequential fragmentation/transport-theory applied to volcanic ash," *J. Geophys. Res.*, vol. 94, no. B11, pp. 15703–15721, doi: 10.1029/JB094iB11p15703, 1989.

[45] Pappalardo G., Mona L., D'Amico G., Wandinger U., Adam M., Amodeo A., Ansmann A., Apituley A., Alados Arboledas L., D. Balis, A. Boselli, J. A. Bravo-Aranda, A. Chaikovsky, A. Comeron, J. Cuesta, F. De Tomasi, V. Freudenthaler, M. Gausa, E. Giannakaki, H. Giehl, A. Giunta, I. Grigorov, S. Groß, M. Haeffelin, A. Hiebsch, M. Iarlori, D. Lange, H. Linne, F. Madonna, I. Mattis, R.-E. Mamouri, M. A. P. McAuliffe, V. Mitev, F. Molero, F. Navas-Guzman, D. Nicolae, A. Papayannis, M. R. Perrone, C. Pietras, A. Pietruczuk, G. Pisani, J. Preißler, M. Pujadas, V. Rizi, A. A. Ruth, J. Schmidt, F. Schnell , P. Seifert , I. Serikov , M. Sicard , V. Simeonov , N. Spinelli , K. Stebel , M. Tesche , T. Trickl , X. Wang, F. Wagner, M. Wiegner, and K. M. Wilson, "Four-dimensional distribution of the 2010 Eyjafjallajo ̈kull volcanic cloud over Europe observed by EARLINET", Atmos. Chem. Phys., 13, 4429–4450, 2013 doi:10.5194/acp-13-4429-2013;

[46] Winker D., "Accounting for multiple-scattering in retrieval from space lidar", 2th International Workshop on Lidar Multiple Scattering Experiments, Christian Werner, Ulrich G. Oppel, Tom Rother, Editors, SPIE Vol. 5059, 2003;

[47] Bissonnette, L.R., 2005. Lidar and multiple scattering. In: Weitkamp, C. (Ed.), LIDAR Range-Resolved Optical Remote Sensing of the Atmosphere. Springer, NY, USA, pp. 43e103.

[48] Rolf C, Kramer M., Schiller C., Hildebrandt M. and M. Riese, "Lidar observation and model simulation of a volcanic-ash-induced cirrus cloud during the Eyjafjallajokull eruption", Atmos. Chem. Phys., 12, 10281–10294, doi: 10.5194/acp-12-10281-2012.

[49] Mori S. and Marzano F. S., "Microphysical characterization of free space optical link due to hydrometeor and fog effects", Vol. 54, No. 22, August 2015/Applied Optics.

[50] Pappalardo G., Amodeo A., Apituley A., Comeron A., Freudenthaler V., Linné H., Ansmann A., Bösenberg J., D'Amico G., Mattis I., Mona L., Wandinger U., Amiridis V., Alados-Arboledas L., Nicolae D. and Wiegner M., ""EARLINET: towards an advanced sustainable European aerosol lidar network", Atmos. Meas. Tech., 7, 2389–2409, doi: 10.5194/amt-7-2389-2014.

[51] Bringi V. N. and Chandrasekar V., *Polarimetric doppler weather radar*, Cambridge University Press, 2004.

[52] Wielaard D. J., Mishchenko M. I., Macke A. and Carlson B. E., "Improved T-matrix computations for large, nonabsorbing and weakly absorbing nonspherical particles and comparison with geometrical-optics approximation", Applied Optics, Vol. 36, No. 18, 1997.

Luigi Mereu was awarded a M.Sc. degree in telecommunication engineering in 2012, and a Ph.D. degree in Remote Sensing in 2016, both from the Sapienza University of Rome, Italy. In 2012, he joined the Department of Information Engineering at Sapienza University of Rome, Italy and the Centre of Excellence CETEMPS in L'Aquila to cooperate on radar remote sensing of volcanic ash clouds within the ICT Ph.D. program. He is involved in the FUTUREVOLC European project started in 2012 and the Aphorism European project started in 2014. He received the IEEE GRS South Italy award for the Best Master Thesis in remote sensing in 2012. He was Visiting Student at the Icelandic Meteorological Office, Reykjavik in 2014; at the Istituto Nazionale di Geofisica e Vulcanologia-Osservatorio Etneo, Catania in 2015.

Simona Scollo was awarded a degree (with Hons.) in Physics (2002) at the University of Catania and a Ph.D. degree (2006) in "Physical Modelling for Environmental Protection" at the Università Alma Mater Studiorum of Bologna. She is a researcher at the Istituto Nazionale di Geofisica e Vulcanologia, Osservatorio Etneo. Her current research focuses on the analysis of the dispersal and fallout processes of eruptive plumes during explosive eruptions; calibration, sensitivity analysis and uncertainty estimation of ash dispersal models; laboratory and field experiments; development of a multidisciplinary system for the detection and monitoring of volcanic plumes and analysis of explosive activity using different remote sensing techniques (e.g. radar, lidar, satellites). She was Visiting Scientist at the University of Geneva in 2015; at the Dipartimento of di Fisica, Università di Federico II, Napoli, Italy in 2011; at the Jet Propulsion Laboratory (NASA), Pasadena, USA in 2010; at the Barcellona Supercomputer Center in 2008; at the Joint Research Centre, Ispra, in 2005; at the Department of Geology and Geophysics School of Ocean and Earth Science and Technology at Manoa, Hawaii in 2003 and 2005.
Dr. S. Scollo has published 35 papers in refereed International Journals, more than 80 presentations at international conferences and workshops. She was the Editor of a Special Issue in Atmospheric Emissions from Volcanoes, Scientific Committee for FisMat 2015, and co-convenor and chairman in different sessions of EGU and IUGG; she is referee for several International Journals. She coordinated several projects and one of them, the VAMOS SEGURO project, was selected in 2012 as a "best practice" among several European Cooperation Projects. In 2011, she obtained the Rittmann medal for young researchers in volcanology and in 2010 the paper Scollo et al. (2010) was selected for the "AGU Research Spotlight".

Saverio Mori (S'05–M'10) was awarded a degree in telecommunications engineering from the University of Florence, Florence, Italy, in 2005 and a Ph.D. degree in remote sensing of environment from the University of Basilicata, Potenza, Italy, and the University of Rome "La Sapienza," Rome, Italy, in 2011, through a joint program. After receiving his degree from the University of Florence, he joined its Satellite Remote Sensing Laboratory. Since 2007, he has been with CETEMPS, University of L'Aquila, Italy, and the Department of Information Engineering, Electronics and Telecommunications (DIET), Sapienza University of Rome, as a Research Scientist. His research activities involve analysis and modeling of atmospheric effects on spaceborne synthetic aperture radars response and on optical propagation along terrestrial links, radiative transfer modeling of scattering media, radar meteorology. Mori was the recipient of the award for the five best Italian degree theses in remote sensing from the IEEE Geoscience and Remote Sensing Society, South Italy Chapter, in 2006.

Antonella Boselli was awarded a degree in Physics from the University of Naples "FedericoII" in 1994. She has been a permanent researcher at the Institute of Methodologies for Environmental Analysis (IMAA) of the National Research Council since December 2001. Her main research interests are in the field of chemical and physical characterization of the atmosphere with laser remote-sensing systems (LIDAR). Her research activity includes optical and microphysical characterization of atmospheric aerosol, also rising from large-scale transport phenomena, with particular reference to Saharan dust and volcanic ash transport events, analysis of multiple scattering processes and depolarization effects on lidar signals, validation of satellite data with lidar data and their integration with model results and in-situ measurement. She was also involved in developing several advanced lidar systems using different spectral region from UV to IR. She has participated in several national and international projects. She has authored and co-authored more than 30 papers in refereed International Journals

Giuseppe Leto was awarded a degree in Physics (1990) and a Ph.D. degree (1995) from the University of Catania. In 1994, he was selected by the Italian Space Agency, Rome, Italy, for a post-doctorate grant in "Research in Infrared Astronomy". From 1995 to 1999, he was appointed as Researcher of the Italian CNR working at the Radioastronomy Institute in Noto, Italy. In 1998-1999, he was a visiting Astronomer at the Center for Astrophysics and Space Astronomy (CASA) of the Colorado University at Boulder (CO, USA). In 1999, he was appointed Astronomer at the Catania Astrophysical Observatory of the Italian National Institute for Astrophysics (INAF). Since 2006, Dr. Giuseppe Leto has been responsible for the INAF "M. G. Fracastoro" Observatory located on Mount Etna. Dr. Giuseppe Leto has experience in laboratory research on materials of interest for astrophysics, observational astronomy, computational astronomy, coordination of teams and observing facilities; he has also been a tutor for bachelor and PHD theses and young astronomer grants. He has been part of a number of projects funded by MIUR, ASI and EC; among them VAMOS SEGURO (VS), a "best practice" EC project oriented to test a LIDAR on Etna plumes. In VS, he served as INAF-PI. Dr. G. Leto has published more than 150 papers, 80 of them in refereed International Journals.

Frank S. Marzano [S'89-M'99-SM'03-F'16] was awarded a degree (with Hons.) in Electrical Engineering (1988) and a Ph.D. degree (1993) in Applied Electromagnetics, both from the University of Rome "La Sapienza", Italy. In 1992, he was a visiting scientist at Florida State University, Tallahassee, FL. During 1993, he collaborated with the Institute of Atmospheric Physics, National Council of Research (CNR), Rome, Italy. From 1994 to 1996, he was with the Italian Space Agency, Rome, Italy, as a post-doctorate researcher. After being a lecturer at the University of Perugia, Italy, in 1997 he joined the Department of Electrical Engineering, University of L'Aquila, Italy teaching courses on electromagnetic fields as Assistant Professor. In 1999, he was at the Naval Research Laboratory, Monterey, CA, as a visiting scientist. In 2002, he qualified as Associate Professor and has co-founded the Center of Excellence on Remote Sensing and Hydro-Meteorological Modeling (CETEMPS), L'Aquila. In 2005, he joined the Dept. of Information engineering, Electronics and Telecommunications, Sapienza Univ. of Rome, Italy where he currently teaches courses on antennas, propagation and remote sensing. Since 2007, he has been vice-director of CETEMPS of the University of L'Aquila, Italy where he was nominated director in March 2013. His current research concerns passive and active remote sensing of the atmosphere from ground-based, airborne, and space-borne platforms and electromagnetic propagation studies. Dr. Marzano has published more than 130 papers in refereed International Journals, more than 30 contributions to international book chapters and more than 300 extended abstracts on international and national congress proceedings. He was the Editor of 2 books. From January 2004 until June 2014, he was an *Associated Editor* of IEEE Geoscience Remote Sensing Letters (GRSL) and since mid-2014 he has been *Associated Editor* of IEEE Transactions on Geoscience and Remote Sensing (TGRS). In 2005 and 2007, he was Guest Co-Editor of the MicroRad04 and MicroRad06 Special Issues for IEEE-TGRS. Since January 2011, he has been Associate Editor of the journal EGU Atmospheric Measurements Techniques. Dr. Marzano has been Fellow of RMetS (Royal Meteorological Society) since 2012 and Fellow of IEEE since 2015.

LIST OF FIGURES AND TABLES

Table I. Overview of supervised ash class parameterization with the list of the main variables and their assumed statistical characterization either derived from literature or heuristically determined. Note: PDF stands for probability density function (U: Uniform), PSD for particle size distribution (PSD), Δx for range variability of x parameter, m_x for mean of x and σ_x for standard deviation of x, AR for particle aspect ratio (see [17] for details).

Ash Particle Ensemble Property	*Very Fine Ash (VA)*	*Fine Ash (FA)*	*Coarse Ash (CA)*	*Small Lapilli (SL)*	*Large Lapilli (LL)*
Ash diameter Variability range ΔD_n (μm)	*Uniform PDF* ΔD_n 2^{-3}-2^{3} 0.125-8	*Uniform PDF* ΔD_n 2^{3}-2^{6} 8-64	*Uniform PDF* ΔD_n 2^{6}-2^{9} *64-512*	*Uniform PDF* ΔD_n 2^{9}-2^{12} 512-4096	*Uniform PDF* ΔD_n 2^{12}-2^{15} 4096-32768
Ash particle concentration Variability range UC: ΔC_p (mg/m^3)	*Uniform PDF* ΔC_p =10^{-3}-10^{4}	*Uniform PDF* ΔC_p =10^{-3}-10^{4}	*Uniform PDF* ΔC_p =10^{-3}-10^{4}	*Uniform PDF* ΔC_p =10^{-3}-10^{4}	*Uniform PDF* ΔC_p =10^{-3}-10^{4}
VC: Very Small Conc.	VC: 10^{-3}-10^{0}	VC: 10^{-3}-10^{0}	VC: 10^{-3}-10^{0}	VC: 10^{-3}-10^{0}	VC: 10^{-3}-10^{0}
SC: Small Conc.	SC: 10^{0}-10^{2}	SC: 10^{0}-10^{2}	SC: 10^{0}-10^{2}	SC: 10^{0}-10^{2}	C: 10^{0}-10^{2}
MC: Medium Conc.	MC: 10^{2}-10^{3}	MC: 10^{2}-10^{3}	MC: 10^{2}-10^{3}	MC: 10^{2}-10^{3}	MC: 10^{2}-10^{3}
IC: Intense Conc.	IC: 10^{3}-10^{4}	IC: 10^{3}-10^{4}	IC: 10^{3}-10^{4}	IC: 10^{3}-10^{4}	IC: 10^{3}-10^{4}
Ash size distribution shape parameter μ_p (adimensional)	*Scaled Gamma PSD* μ_p = *1-2* *U-PDF*	*Scaled Gamma PSD* μ_p = *1-2* *U-PDF*	*Scaled Gamma PSD* μ_p = *1-2* *U-PDF*	*Scaled Gamma PSD* μ_p = *1-2* *U-PDF*	*Scaled Gamma PSD* μ_p = *1-2* *U-PDF*
Ash particle density ρ_p (g/cm^3)	*Uniform PDF* ρ_p = *0.5-2.5*	*Uniform PDF* ρ_p = *0.5-2.5*	*Uniform PDF* ρ_p = *0.5-2.5*	*Uniform PDF* ρ_p = *0.5-2.5*	*Uniform PDF* ρ_p = *0.5-2.5*
Ash particle canting angle mean and deviation $m_\square$ (°) and $\sigma_\square$ (°) *TO.1: Tumbling Orientation, TO.2: Tumbling Orientation, TO.3: Tumbling Orientation, OO: Oblate Orientation PO : Prolate Orientation*	*TO.1: G-PDF* m_ϕ=30°;σ_ϕ=30° *TO.2: G-PDF* μ_ϕ=45°;σ_ϕ=30° *TO.3: G-PDF* μ_ϕ=60°;σ_ϕ=30° *OO: G-PDF* μ_ϕ=0°;σ_ϕ=10° *PO: G-PDF* μ_ϕ= 90°; σ_ϕ=10°	*TO.1: G-PDF* m_ϕ=30°; σ_ϕ=30° *TO.2: G-PDF* μ_ϕ=45°; σ_ϕ=30° *TO.3: G-PDF* μ_ϕ=60°; σ_ϕ=30° *OO: G-PDF* μ_ϕ=0°; σ_ϕ=10° *PO: G-PDF* μ_ϕ= 90°; σ_ϕ=10°	*TO.1: G-PDF* μ_ϕ=30°; σ_ϕ=30° *TO.2: G-PDF* μ_ϕ=45°; σ_ϕ=30° *TO.3: G-PDF* μ_ϕ=60°; σ_ϕ=30° *OO: G-PDF* μ_ϕ=0°; σ_ϕ=10° *PO: G-PDF* μ_ϕ= 90°; σ_ϕ=10°	*TO.1: G-PDF* μ_ϕ=30°; σ_ϕ=30° *TO.2: G-PDF* μ_ϕ=45°; σ_ϕ=30° *TO.3: G-PDF* μ_ϕ=60°; σ_ϕ=30° *OO: G-PDF* μ_ϕ=0°; σ_ϕ=10° *PO: G-PDF* μ_ϕ= 90°; σ_ϕ=10°	*TO.1: G-PDF* μ_ϕ=30°; σ_ϕ=30° *TO.2: G-PDF* μ_ϕ=45°; σ_ϕ=30° *TO.3: G-PDF* μ_ϕ=60°; σ_ϕ=30° *OO: G-PDF* μ_ϕ=0°; σ_ϕ=10° *PO: G-PDF* μ_ϕ= 90°; σ_ϕ=10°
Non-spherical particle axial ratio r_{ax} : axis ratio [adim] RB: basaltic ratio RR: rhyolitic ratio	r_{ax}=*AR* *RB:* $r_{ax\text{-}b}$ *RR:* $r_{ax\text{-}r}$	r_{ax}=*AR* *RB:* $r_{ax\text{-}b}$ *RR:* $r_{ax\text{-}r}$	r_{ax}=*AR* *RB:* $r_{ax\text{-}b}$ *RR:* $r_{ax\text{-}r}$	r_{ax}=*AR* *RB:* r_{ax} =*1.4* *RR:* r_{ax} =*2.4*	r_{ax}=*AR* *RB:* r_{ax} =*1.4* *RR:* r_{ax} =*2.4*
Optical dielectric constant for volcanic ash	*Uniform PDF*	*Uniform PDF*	*Uniform PDF*	*Uniform PDF*	*Uniform PDF*

Table II. Percentage ratio between the standard deviation ($\sigma_{Ca}/\langle C_a\rangle$, $\sigma_{Dn}/\langle D_n\rangle$) as well as overall MS-included standard deviation ($\sigma_{CaMS}/\langle C_a\rangle$, $\sigma_{DnMS}/\langle D_n\rangle$) with respect to the average retrieved value for both concentration and mean diameter, respectively, considering various f_{MS} (0, 0.1, 0.2 and 0.3) for 3 cases: a) at three elevations during the 15 November 2010 eruption (using the depolarization measurements); b) during the Etna eruption on 12 August 2011 (using the depolarization measurements); c) profile of ash plume on 12 August 2011 (using the full dataset).

	Altitude [m]	Uncertainty [%]	f_{MS} = 0	f_{MS} = 0.1	f_{MS} = 0.2	f_{MS} = 0.3
a)	**300**	$\sigma_{Ca}/\langle C_a\rangle$	39.44	-	-	-
		$\sigma_{CaMS}/\langle C_a\rangle$	-	42.70	41.98	41.04
		$\sigma_{Dn}/\langle D_n\rangle$	3.83	-	-	-
		$\sigma_{DnMS}/\langle D_n\rangle$	-	5.65	5.98	5.96
	400	$\sigma_{Ca}/\langle C_a\rangle$	82.75	-	-	-
		$\sigma_{CaMS}/\langle C_a\rangle$	-	89.28	88.23	84.30
		$\sigma_{Dn}/\langle D_n\rangle$	9.88	-	-	-
		$\sigma_{DnMS}/\langle D_n\rangle$	-	14.23	14.78	14.93
	500	$\sigma_{Ca}/\langle C_a\rangle$	41.14	-	-	-
		$\sigma_{CaMS}/\langle C_a\rangle$	-	45.25	44.62	42.95
		$\sigma_{Dn}/\langle D_n\rangle$	4.17	-	-	-
		$\sigma_{DnMS}/\langle D_n\rangle$	-	6.22	6.47	6.39
	Elevation [deg]	**Uncertainty [%]**	f_{MS} = 0	f_{MS} = 0.1	f_{MS} = 0.2	f_{MS} = 0.3
b)	**20-59**	$\sigma_{Ca}/\langle C_a\rangle$	4.41	-	-	-
		$\sigma_{CaMS}/\langle C_a\rangle$	-	6.13	5.87	5.57
		$\sigma_{Dn}/\langle D_n\rangle$	8.33	-	-	-
		$\sigma_{DnMS}/\langle D_n\rangle$	-	12.77	12.21	11.81
	Elevation [deg]	**Uncertainty [%]**	f_{MS} = 0	f_{MS} = 0.1	f_{MS} = 0.2	f_{MS} = 0.3
c)	**Profile**	$\sigma_{Ca}/\langle C_a\rangle$	1.22	-	-	-
		$\sigma_{CaMS}/\langle C_a\rangle$	-	1.22	1.22	1.22
		$\sigma_{Dn}/\langle D_n\rangle$	4.68	-	-	-
		$\sigma_{DnMS}/\langle D_n\rangle$	-	7.55	6.78	7.10

Table III: Mean value (Mean) and standard deviation (Std) of the VALR-ML estimates of very-fine-ash (VA) concentration and mean diameter during the Etna lava fountain on 12 August 2011 considering the HAPESS simulated dataset with both spheroidal and spherical particles (complete) and without spherical particles (partial).

	DataSet (VA)	Elevation range [°]	Concentration [mg/m^3]	Mean diameter [μm]	Detected ash classes and occurrence
LIDAR estimates using VALR-ML	OO, PO, TO, MC, SC, VC	20-59	Mean: 67.46 Std: 37.84	Mean: 2.89 Std: 1.18	VA-OO: 31 VA-PO: 79 VA-TO: 31
	OO, PO, TO, MC, SC, VC + SP	20-59	Mean: 62.52 Std: 36.84	Mean: 3.13 Std: 1.27	VA-OO: 21 VA-PO: 49 VA-SP: 52 VA-TO: 19

Table IV: Contingency table related to ash concentration map at three elevations during the 15 November 2010 Etna ash emission, related to three different concentration thresholds (see text for details).

		PARAMETRIC RETRIEVAL MODEL (PM1)					
	H	Th_1=2*10^{-4} [g/m^3]		Th_2=2*10^{-3} [g/m^3]		Th_3=4*10^{-3} [g/m^3]	
VALR-ML ALGORITHM	**300**	HIT: 97.38%	MISS: 0%	HIT: 54.90%	MISS: 11.11%	HIT: 47.71%	MISS: 16.33%
		FALSE: 2.62%	NEG: 0%	FALSE: 21.56%	NEG: 12.41%	FALSE: 15.68%	NEG: 20.26%
	400	HIT: 96.92%	MISS: 0%	HIT: 52.30%	MISS: 2.46%	HIT: 49.23%	MISS: 2.47%
		FALSE: 3.08%	NEG: 0%	FALSE: 36.30%	NEG: 8.92%	FALSE: 26.77%	NEG: 21.53%
	500	HIT: 95.93%	MISS: 0%	HIT: 67.44%	MISS: 4.07%	HIT: 65.70%	MISS: 5.81%
		FALSE: 4.07%	NEG: 0%	FALSE: 26.16%	NEG: 2.32%	FALSE: 20.93%	NEG: 7.55%

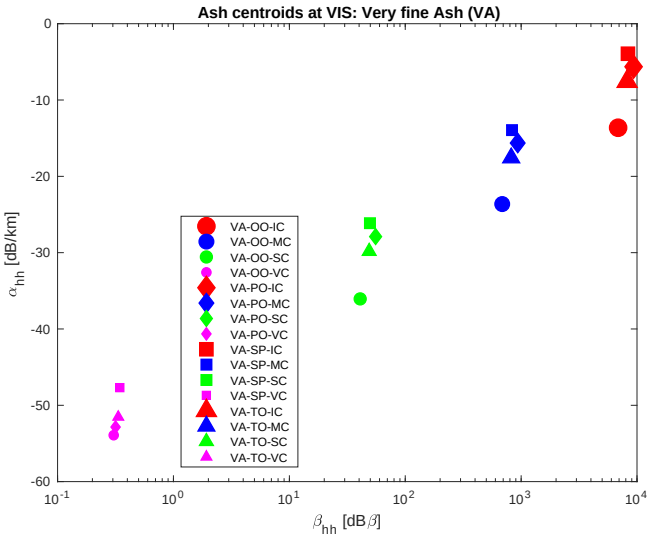

Figure 1. Correlation between backscattering (in dBβ) and extinction coefficient (in dB/km) for the VA size class in terms of ash concentration and orientation class centroid noting that, as the concentration increases, there is an increase of the simulated backscattering and extinction coefficients.

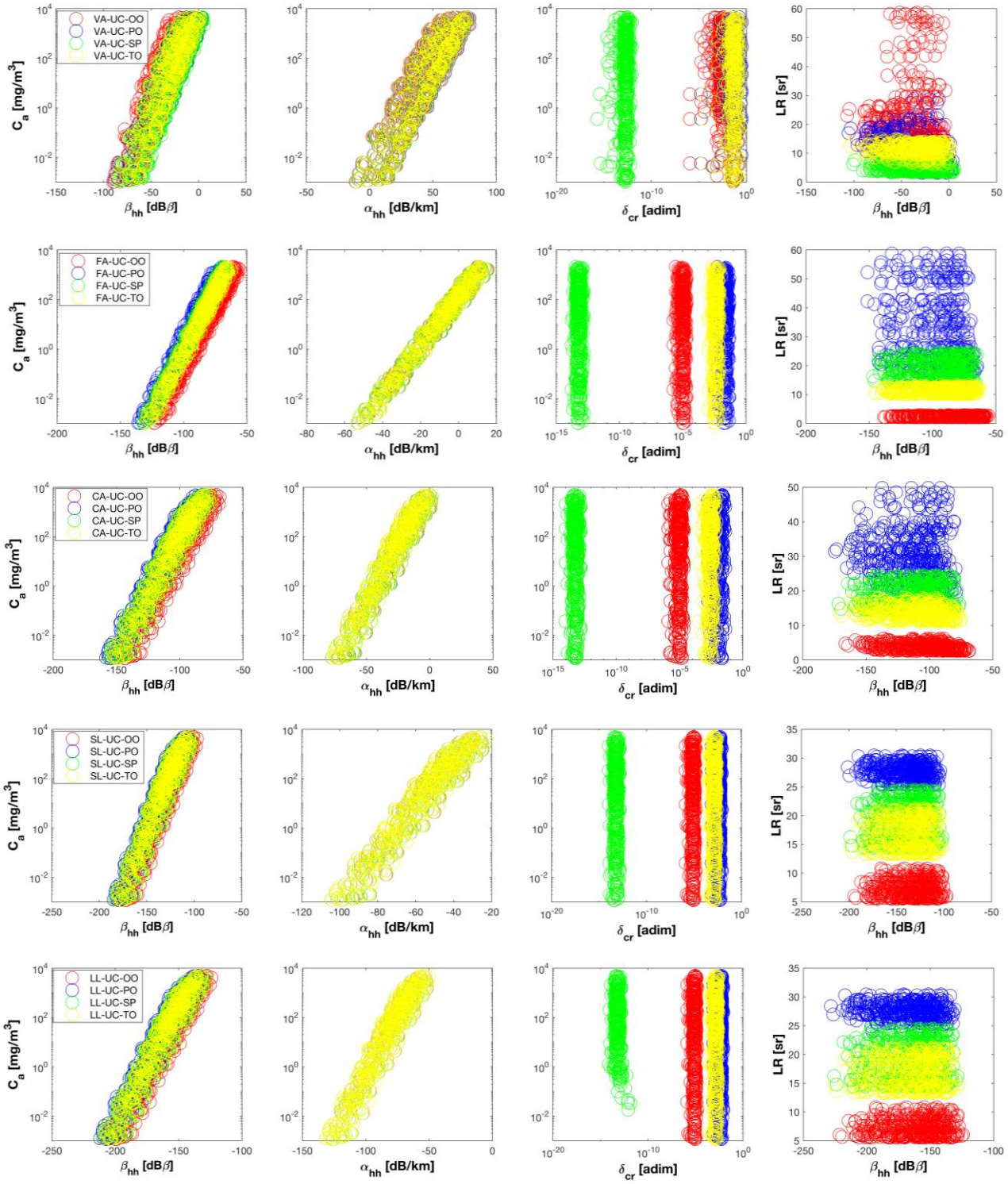

Figure 2. Numerical results of the HAPESS simulations at 532 nm wavelength (VIS). Correlation between ash mass concentration C_a (mg/m^3) and both backscatter (in dBβ) and extinction coefficients (in dB/km) in the upper panels (left and right panels, respectively) and between Lidar Ratio (LR) and backscatter and between ash mass concentration C_a (mg/m^3) and cross polarization in the lower panels (left and right panels, respectively), for each ash class VA, FA, CA, SL and LL (2x2 panels), for different orientations (OO, PO, SP TO) and uniform concentration (UC) (between 1 - 10^7 μg/m^3). See text and Table I for details.

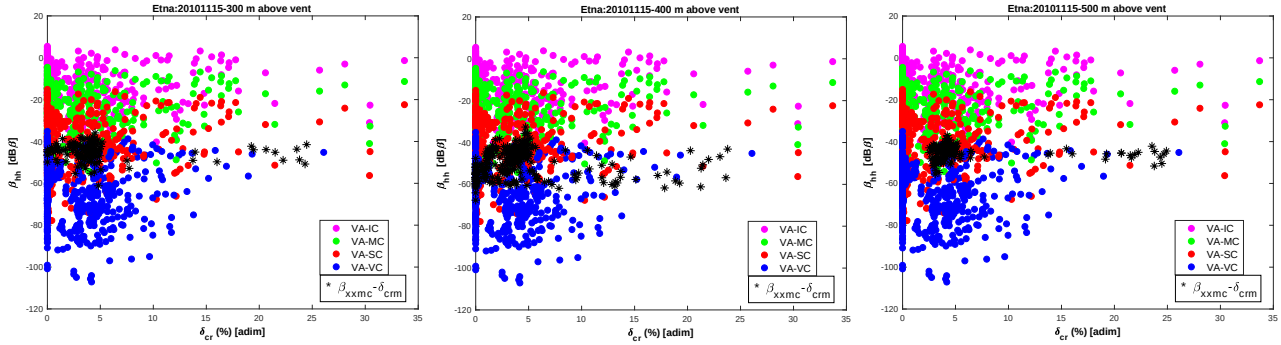

Figure 3. Lidar data collected during the 15 November 2010 ash emission at Mt. Etna, in Italy. Superimposition between measured (dark dots) and simulated backscatter coefficient β_{hh} (in dBβ) and cross-polarization ratio δ_{cr} (in %) at 300 (left panel), 400 (middle panel) and 500 m (right panel) of altitude above Etna summit craters, respectively. The different color identifies different concentration classes (IC in magenta, MC in green, SC in red and VC in blue), all for the very fine ash class (VA).

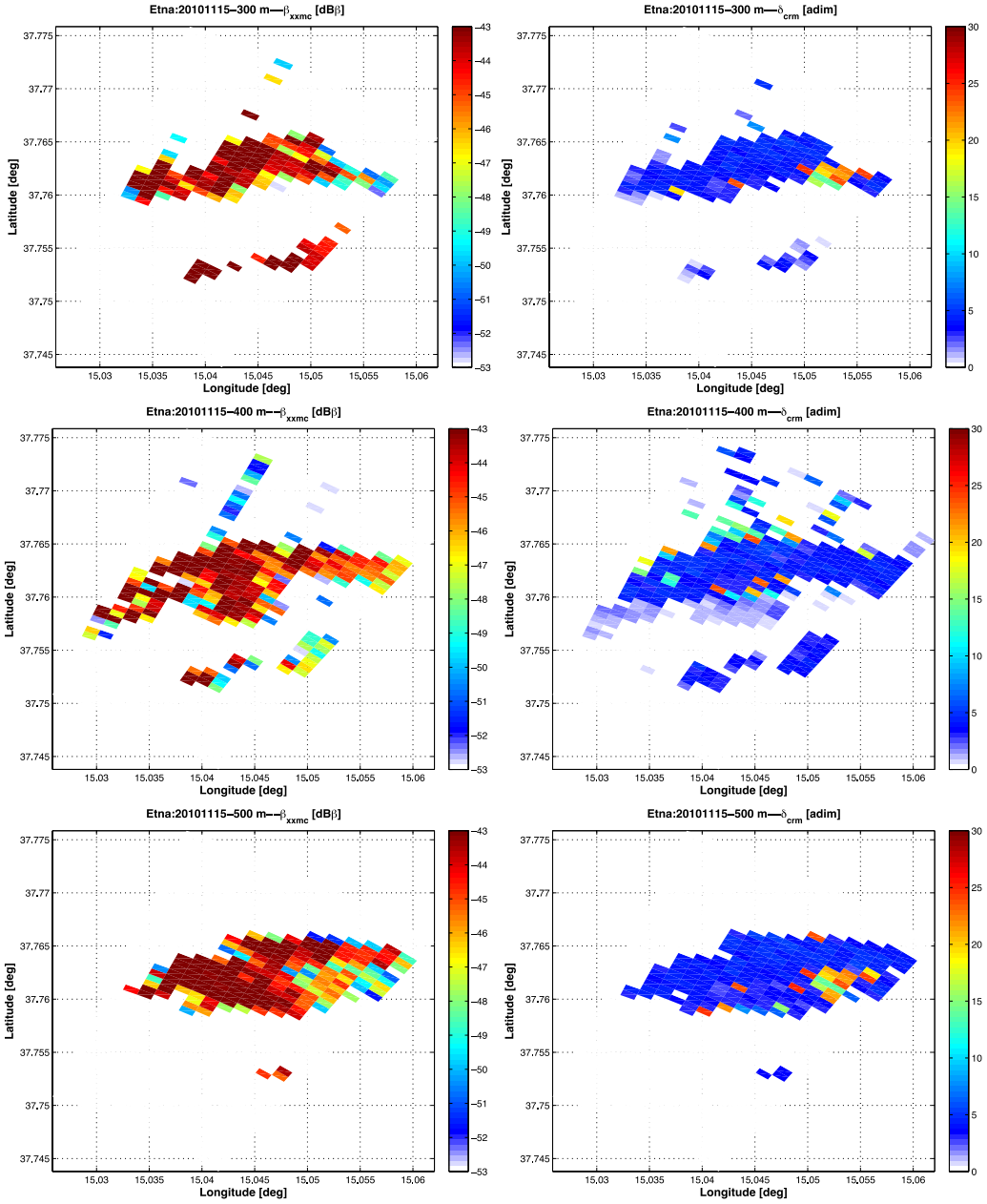

Figure 4. Lidar data collected during the 15 November 2010 ash emission at Mt. Etna, in Italy. Maps of the measured backscatter coefficient (in dBβ) and linear volumetric depolarization (in %), left and right panels respectively, at each elevation (300, 400 and 500 m) above the Etna summit craters.

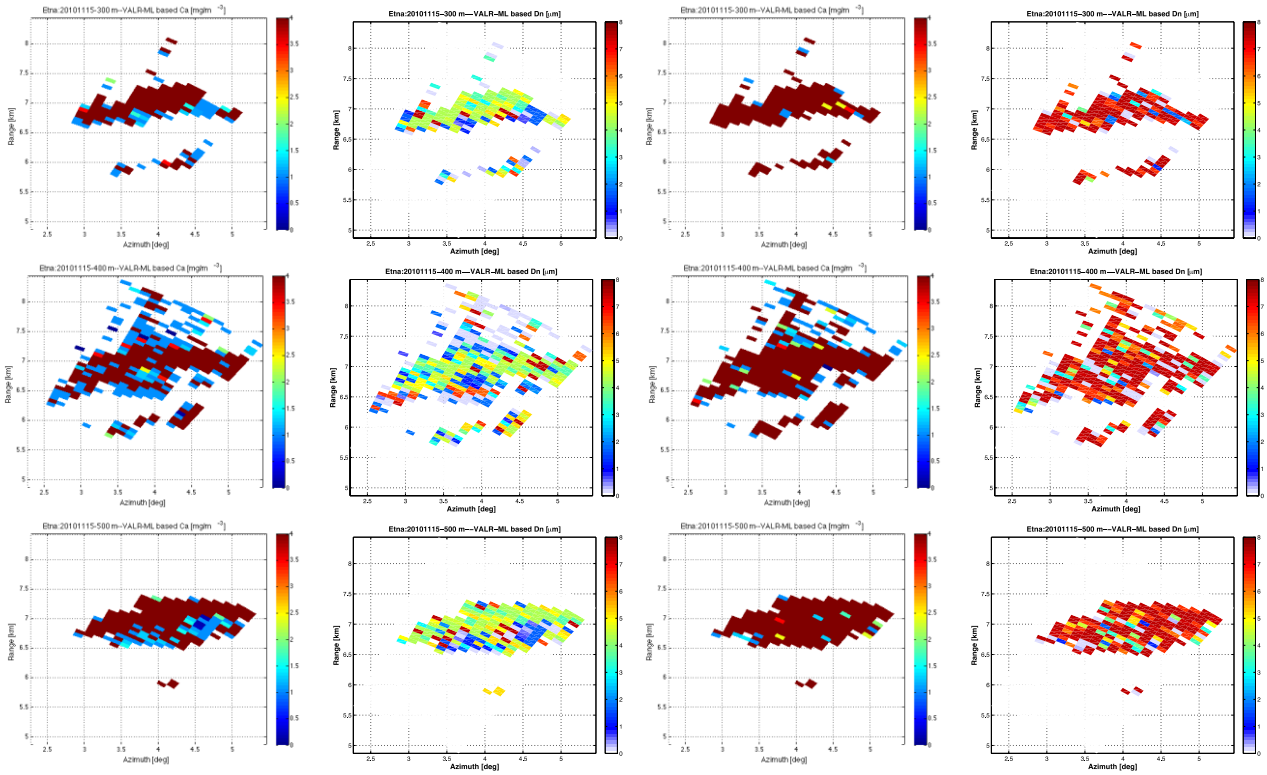

Figure 5. Mt. Etna eruption on 15 November 2010. Maps of VALR-ML estimates of ash concentration and mean diameter at each elevation at 300, 400 and 500 m (first, second and third rows, respectively) above the summit crater of Mt. Etna using: 1) both measured lidar observables β_{xxmc} and δ_{crm} (first two columns on the left); 2) only the backscatter coefficient β_{xxmc} (last two columns on the right).

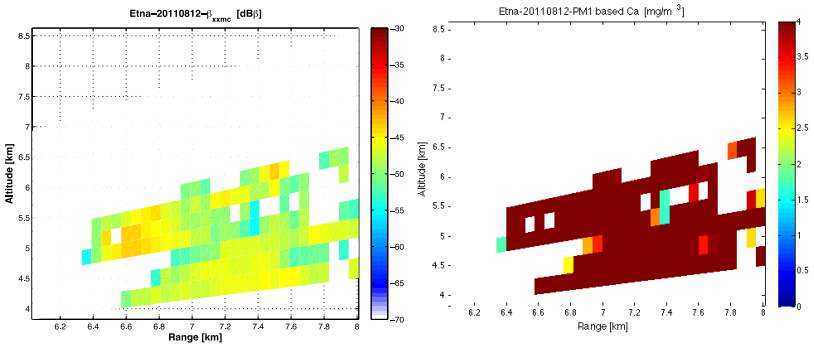

Figure 6. Lidar data collected during the 12 August 2011 lava fountain event at Mt. Etna, in Italy. (Left panel) Cross section of the measured backscatter coefficient (in dBβ) of ash plume as a function of altitude above the craters and range. PM1 retrieval of ash concentration considering a r_{eff}=10μm (Right panel).

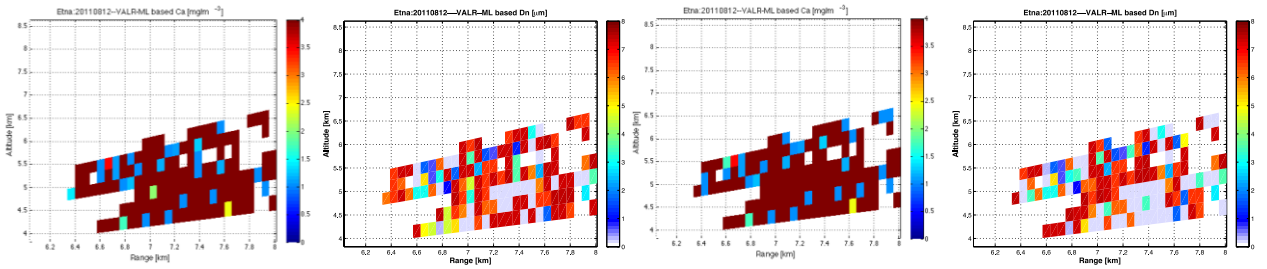

Figure 7. Lidar data collected during the lava fountain event on 12 August 2011 at Mt. Etna (Italy). Cross sections of VALR-ML estimates of ash concentration and mean diameter, respectively, considering a complete HAPESS simulation dataset (two panels on the left) and a partial simulation dataset without spherical particles (two panels on the right).

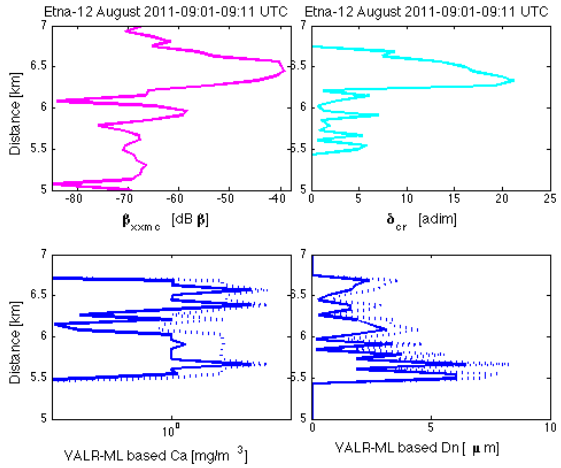

Figure 8. Lidar data collected at 09:01-09:11 UTC during the 12 August 2011 lava fountain event at Mt. Etna, in Italy. (Upper panels) Range profiles of ash backscattering and depolarization measured by the VAMP system at Serra La Nave station. (Lower panels) VALR-ML estimated ash concentration and mean diameter (solid curve) together with the same estimates plus its standard deviation (dashed curve) derived from (12).

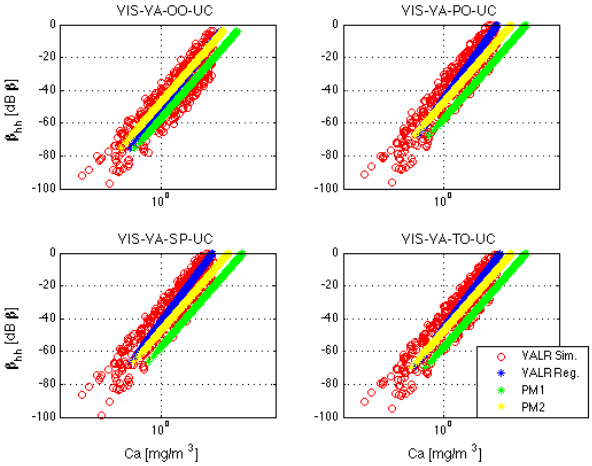

Figure 9. Correlation between the backscatter coefficient (in dBβ) and the ash concentration (in g/m^3) derived from i) the HAPESS simulations (red dots) referring to very fine ash (VA) ash class with OO, PO, SP, TO orientation (see title of each panel); ii) parametric models VALR-Reg (blue dots), PM1 (yellow dots) and PM2 (green dots), respectively.

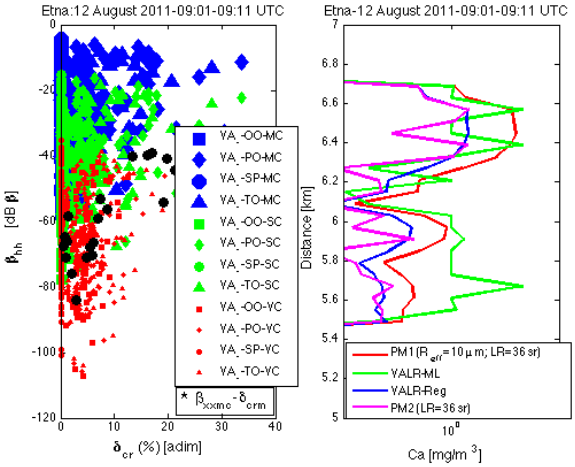

Figure 10. Etna eruption on 12 August 2011 at 09:01-09:11 UTC. (Left panel) Comparison between the simulated (colored dots for each considered class in Table I) and measured backscatter coefficient (black dot, in dBβ) and cross-polarization ratio (black dots, in %). (Right panel) Profile of the concentration estimates derived from PM1 (with effective radius equal to 10 µm), PM2, VALR-Reg and VALR-ML algorithms.

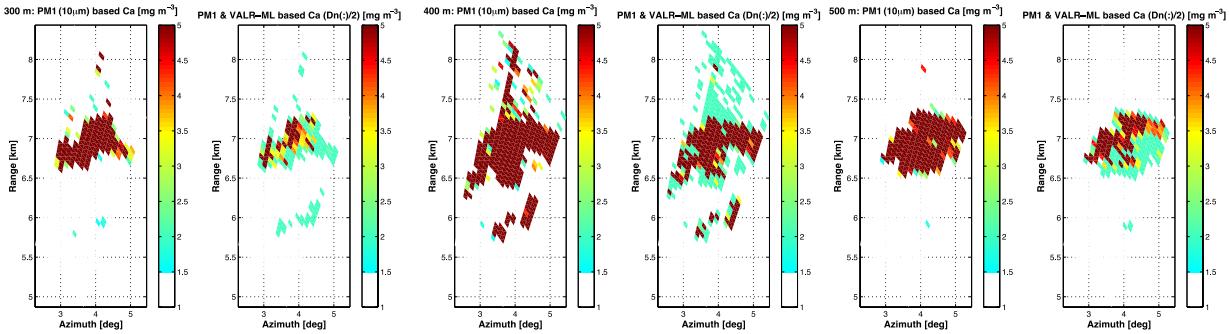

Figure 11. Etna eruption on 15 November 2010. Panels (first, second and third couple of plots) are related to elevations at 300, 400 and 500 m above the Etna summit craters. Ash concentration derived by the PM1 retrieval using: i) (left panel of each couple of plots) an ash effective radius of 10 μm as in [33]; ii) (right panel of each picture) the mean radius derived from the VALR-ML retrieval for each detected pixel as shown in Fig. 5.

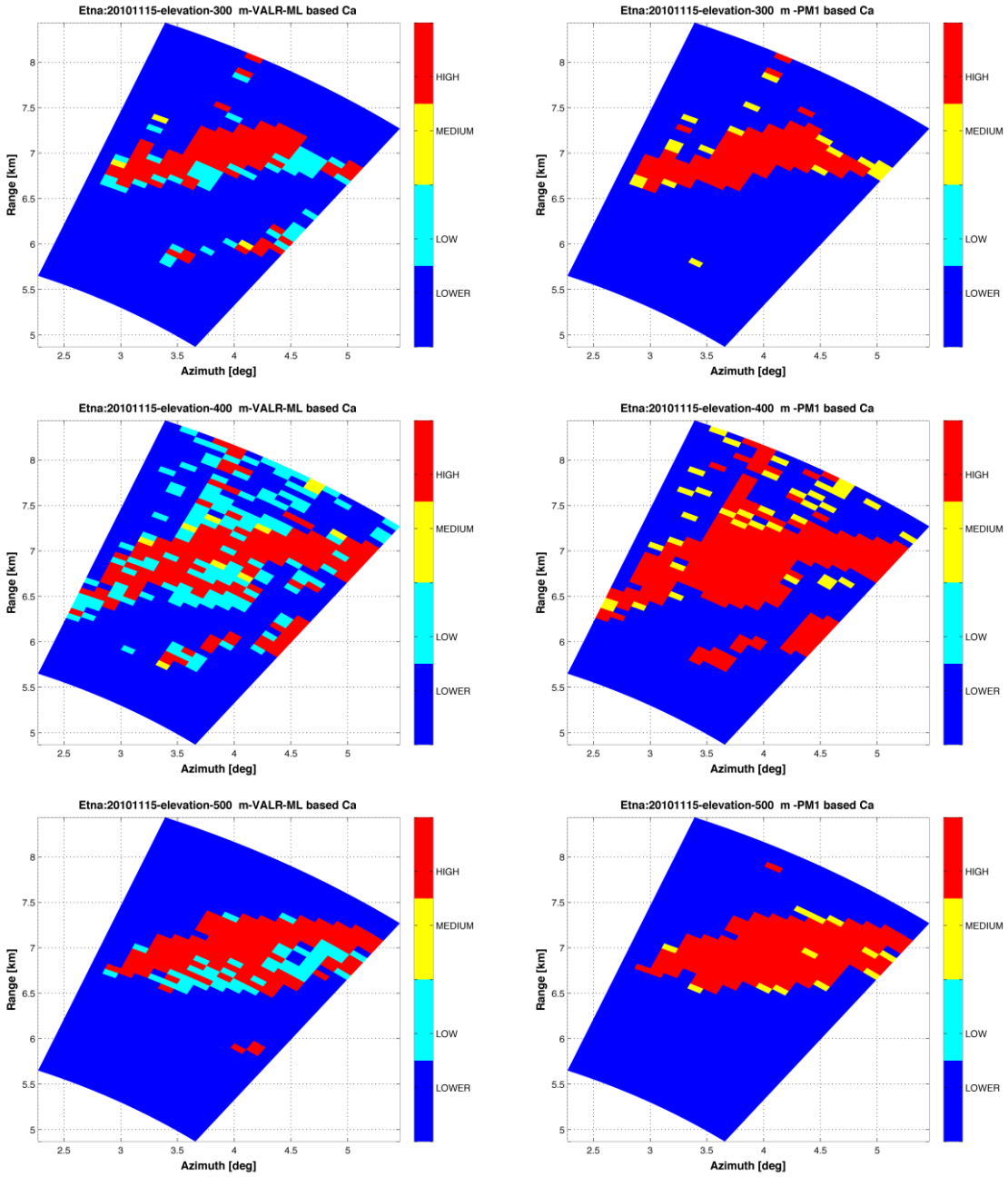

Figure 12. Etna eruption on 15 November 2010. Ash concentration range maps obtained applying the VALR-ML and PM1 derived mass concentration, on the left and on the right respectively, and referred to 300, 400 and 500 m of elevation. The different colors identify the area of LOWER ($<2\cdot10^{-4}$ g/m^3), LOW ($2\cdot10^{-4}$ g/m^3 - $2\cdot10^{-3}$ g/m^3), MEDIUM ($2\cdot10^{-3}$ g/m^3 - $4\cdot10^{-3}$ g/m^3) and HIGH ($>4\cdot10^{-3}$ g/m^3) ash contamination defined by the ICAO regulations.